 CMES, vol.3, no.5, pp.643-673, 2002

Atomic Modeling of Carbon-Based Nanostructures as a Tool for Developing New Materials and Technologies

D.W. Brenner, O.A. Shenderova, D.A. Areshkin, J.D. Schall[1] and S.-J. V. Frankland[2]

Abstract: The derivation of a bond-order potential energy function and a self-consistent tight-binding scheme is presented, followed by a survey of the application of these methods to calculating properties of carbon nanostructures. The modeling studies discussed include properties of functionalized and kinked carbon nanotubes, Raman shifts for hydrogen stored in nanotubes, nanotubes in a composite, properties of nanotubes in applied potential (electrical) fields, and structures and properties of nanocones, nanodiamond clusters and rods, and hybrid diamond-nanotube structures.

keyword: Molecular dynamics, tight-binding, simulation, nanotube, nanorod, diamond, composites, hydrogen storage.

1 Introduction to Carbon Nanostructures

Carbon-based structures display an amazingly diverse collection of properties. At the macroscopic level, diamond is the most atomically dense and hardest known material. It has an extremely high thermal conductivity (five times that of copper), has a high Debye temperature and melting point, and is relatively chemically inert.[Field (1992)] Progress has also been made in doping diamond for microelectronics applications, and polycrystalline diamond has desirable properties as an electron field emitting material.[Zhirnov (1998)] Bulk graphite has an exceedingly large in-plane elastic modulus, a property that has lead to advanced fiber-reinforced composites with large strength-to-weight ratios. At the same time the weak inter-planar bonding in graphite makes it soft, produces desirable lubrication properties (under appropriate conditions of temperature and humidity), and allows significant ion intercalation, a property useful for battery applications. The properties and applications of carbon-based polymeric materials, not to mention biological structures, are too numerous to list.

At the nanometer scale, carbon-based structures display a no less incredible diversity of properties and potential applications. Fullerene nanotubes, for example, have extremely large moduli that rival (and potentially exceed) that of diamond. [Yacobson (1997)] Fullerene nanotubes can be metallic or semiconducting depending on their radius and helical structure,[Mintmire (1996)] leading to novel mono-elemental metal-semiconductor junctions.[Chico (1996)] Carbon nanotubes are ballistic electron transport media with scattering lengths on the order of microns or more,[White (1998)] and with their large aspect ratio and electronic properties they are proving to be efficient electron emitters.[Zhu (1999)] Fullerene nanotubes may also be doped, and they allow relatively high densities of ion and hydrogen intercalation, properties that potentially impact energy storage applications. Nanodiamond clusters also display desirable electron field-emission properties, [Givargizov (1995)] and they may find applications as novel quantum dots for optoelectronic applications. Compounds based on the C_{60} fullerene structure are also being explored for unique biological activity, and they currently show promise as new treatments for a wide range of diseases, including Acquired Immune Deficiency Syndrome (AIDS) and neurodegenerative disorders such as Amyotrophic Lateral Sclerosis.[Jenson (1996)]

Theory and modeling have played a central role in the development of our understanding of the properties of carbon nanostructures. For example, theory first predicted that fullerene nanotubes can be either semiconducting or metallic depending on their structure, [Mintmire (1992)] a prediction that has been confirmed by experiment. Their high modulus and the formation of kinks due to bending are two more examples of properties that were predicted by theory either before or simultaneous

[1] Department of Materials Science and Engineering
North Carolina State University, Raleigh, NC 27695-7907
[2] M/S 132C ICASE,
NASA Langley Research Center,
Hampton, VA 23669

with experimental measurements. [Iijima (1996)]

Presented in this paper is a survey of our recent atomic-scale modeling studies of carbon-based nanostructures. The intent of each of the studies discussed below is to develop the fundamental knowledge needed to effectively use specific carbon nano-structures in technology applications. Presented in the following section is a brief introduction to the computational tools used in the modeling studies, specifically a many-body analytic potential for predicting structures, energies, stresses, and elastic properties of carbon structures, as well as a self-consistent tight-binding method for predicting electronic properties. Specific modeling studies are discussed in Section III. Some of these studies are on structures that have been realized and are at various stages of being incorporated into new technologies, while others involve structures with potentially unique properties that may have not yet been created. The studies are broken down into three classes of systems, fullerene nanotubes, nanodiamond structures, and hybrid fullerene-diamond systems. The final section contains a short discussion of some of the remaining questions to be answered regarding applications of carbon nanostructures.

2 Modeling Techniques

The studies surveyed below employed primarily two types of atomic-scale modeling. The first is structural and molecular dynamics modeling using an analytic many-body bond-order potential energy function that can be derived from fundamental quantum bonding theory.[Brenner (1990 (2000 (2002)] An outline of how this expression can be obtained from the Harris functional form of density functional theory is given in the following section.[Brenner (1998)] In the second atomic modeling approach, the electronic structure of nanoscale carbon structures is obtained from both traditional tight-binding models and a self-consistent tight-binding formalism. The latter formalism, which is a modification to an environment dependent tight-binding model,[Tang (1996)] allows for charge transfer and the efficient incorporation of applied electric fields into density-functional-based, semi-empirical electronic structure calculations.[Areshkin, (2002)] As discussed in more detail in Section 2.2, the incorporation of self-consistent terms represents a computationally efficient compromise between tight-binding and first-principles approaches to calculating electronic structure. [Demkov (1995); Frauenheim, (2000); Horsfield, (2000)]

2.1 Bond-Order Potential Energy Function: Form and Derivation

The analytic bond-order potential energy function used in the studies discussed below was originally introduced by Abell[Abell (985)] and first applied as a practical potential energy formalism for modeling covalent materials by Tersoff.[Tersoff (1986)] This expression uses an interatomic bond-order function that modulates a two-center interaction to model the local attractive contribution to the binding energy E_i^{el} of an atom i from the valence electrons:

$$E_i^{el} = -\sum_{(j\neq i)} b_{ij} V^A(r_{ij}) \tag{1}$$

Here the sum is over nearest neighbors j of atom i, b_{ij} and r_{ij} are the bond-order function and scalar distance between atoms i and j, respectively, and the two-center function $V^A(r)$ represents interactions from valence electrons. This function is assumed to be transferable between different atomic hybridizations, and all many-body effects are included in the bond-order function. The attractive interactions are balanced with a sum of pair-wise additive repulsive terms $V^R(r)$. This leads to the expression

$$E_{coh} = \sum_i \sum_{(j\neq i)} [V^R(r_{ij}) \quad - \quad \overline{b}_{ij}\, V^A(r_{ij})] \tag{2}$$

for the cohesive energy E_{coh} of a collection of carbon and hydrogen atoms. A screened Coulomb potential and a sum of three exponential functions are used for $V^R(r)$ and $V^A(r)$, respectively.

The many-body bond-order function has the form

$$\overline{b}_{ij} = \frac{[b_{ij}^{\sigma\pi} + b_{ji}^{\sigma\pi}]}{2} + b_{ij}^{\pi} \tag{3}$$

where values for $b_{ij}^{\sigma\pi}$ and $b_{ji}^{\sigma\pi}$ depend on the local bonding environments of atoms i and j, respectively.[Brenner (1990; 2000; 2002)] The primary influence of local bonding environment on the bond-order is through the coordination number such that the value of the bond-order decreases with increasing local coordination. As shown below, tight-binding theory yields the result that the bond-order should decrease as the inverse of the square root

Table 1 : Selected properties for diamond, graphite and hydrocarbon molecules given by the bond-order potential. Sources for the experiment/first principles data values are given in [Brenner (2002)].

Property	***Potential Function***	***Experiment/First Principles Value***	***Property***	***Potential Function***	***Experiment/First Principles Value***
Bulk Diamond Properties					
Lattice constant (Å)	5.43	5.43	C_{11}(Mbar)	10.7	10.8
Bulk Modulus (dynes/cm^2)	4.4x10^{12}	4.4x10^{12}	C_{12}(Mbar)	1.0	1.3
Atomization Energy (eV/atom)	7.36	7.36	C_{44}(Mbar)	6.8	5.8
(111) 1x1 surface energy (eV/atom)	-0.20	-0.37	(111) 2x1 pi-chain surface energy (eV/atom)	-0.77	-0.68
Vacancy Formation (eV)	7.2	7.2	Interstitial (T) (eV)	19.4	23.6
Interstitial (S) (eV)	12.3	16.7	Interstitial (B) (eV)	11.6	15.8
Heats of formation for selected hydrocarbon molecules (in kcal/mole)					
CH_3	35.48	35.8	CH_4	-16.70	-15.99
C_2H_2	53.96	54.33	C_2H_4	13.66	14.52
C_2H_6	-17.31	-16.52	c-C_6H_{12}	-21.29	-20
C_2H	133.42	135	$H_3C_2H_2$	22.77	28.3
1-butyne	48.95	42.8	2-butyne	48.97	38
i-C_4H_9	17.78	19.4	t-C_4H_9	10.11	15.2
n-butane	-22.34	-23.5	i-butane	-22.30	-25.4
Benzene	21.75	24	Naphthalene	37.51	31.04
CH_2	89.86	93.2			

of the coordination. This bond-order model effectively mimics the limited valence electron density that an atom can contribute to the formation of chemical bonds. A secondary factor entering the value of the bond-order are bond angles, where an angular contribution to the coordination is used that favors bond angles to be as close to 180^o as possible. This mimics repulsion between electron pairs in different covalent bonds, and results in structures that agree with electron pair repulsion theory for non-radical species. The function b^{π}_{ij} in Eq.(3) accounts for contributions from pi interactions and the radical character of bonds, and includes whether a bond is part of a conjugated system as well as the value of dihedral angles for carbon-carbon double bonds.

Details of the specific functional forms and parameters used in the analytic potential are given elsewhere.[Brenner (2002)] Selected physical properties described by the potential function are listed in Tab. 1. Within a single expression, the function provides a reasonably accurate description of a rather broad set of properties, including bond lengths, energies and elastic properties of solid state and molecular structures, radical energies and conjugated pi bonding properties, and diamond surface properties. This is a critical set of properties if a reasonable description of diamond, graphitic and hybrid diamond-graphitic structures like those described below are to be modeled.

The form of the analytic bonding expression described above can be derived from density functional theory.[Brenner (1998)] The variational principle of density

functional theory leads to a system of one-electron equations of the form

$$[T + V_H(r) + V_N(r) + V_{XC}(r)]\,\phi_i^{\mathrm{K-S}} = \varepsilon_i\,\phi_i^{\mathrm{K-S}} \tag{4}$$

where ϕ_i^{K-S} are the one-electron Kohn-Sham orbitals, ε_i are the eigenenergies of these orbitals, T is the kinetic energy operator, V_H(r) is the Hartree potential, V_N(r) is the potential energy due to the nuclei and V_{xc}(r), called the exchange-correlation potential, is the functional derivative of the exchange-correlation energy. The matrix elements that determine the Kohn-Sham orbitals are given by

$$\hat{H} = -\frac{\nabla^2}{2} + V_{ext} + \int \frac{\rho(R)}{|r-R|} + V_{xc}[\rho(R)] \tag{5}$$

where V_{ext} is the external potential, which includes the potential energy from the nuclei and any applied fields, and the other terms are as above. These equations can be solved self-consistently to obtain the ground state Kohn-Sham orbitals, and the total electronic energy can be obtained from the expression

$$\mathrm{E}[\rho^{\mathrm{in}}(r)] = \sum_k \varepsilon_k - \int \rho^{\mathrm{SC}} \left[\frac{\mathrm{V_H}(r)}{2} + \mathrm{V_{XC}}(r)\right] \mathrm{dr} + \mathrm{E_{XC}}[\rho^{\mathrm{SC}}(r)] \tag{6}$$

where ρ^{SC} is the self-consistent electron density, ε_k are the eigenvalues of the occupied Kohn-Sham orbitals, and $\mathrm{E_{XC}}$ is the exchange-correlation energy.

Harris [Harris (1985)] as well as Foulkes and Haydock [Foulkes (1989)] demonstrated that the electronic energy calculated from a single iteration of the energy functional

$$\mathrm{E^H}[\rho^{\mathrm{in}}(r)] = \sum_k \varepsilon_k^{\mathrm{out}} - \int \rho^{\mathrm{in}}[\mathrm{V_H}/2 + \mathrm{V_{XC}}(r)]\mathrm{dr} + \mathrm{E_{XC}}[\rho^{\mathrm{in}}(r)] \tag{7}$$

is second-order in the error in charge density. In this expression the superscript "in" refers to an input charge density, and the superscript "out" refers to the occupied orbital energies of the Kohn-Sham orbitals created from this input charge density via Eq.(5). This expression Eq.(7) is generally referred to as the Harris (or sometimes Harris-Foulkes) functional. While the correct input electron density yields the correct ground-state energy, the Harris functional is not variational; it can give energy either higher or lower than the true ground-state energy.

Foulkes and Haydock pointed out that the expression Eq.(7) provides a fundamental basis for understanding why non-self-consistent tight-binding theory can capture much of the electronic properties and even total energies produced by more sophisticated electronic structure methods.[Foulkes (1989)] Tight-binding expressions generally give the total energy E_{tot} for a system of atoms as a sum of eigenvalues of a set of occupied non-self-consistent one-electron molecular orbitals plus some additional analytic function of relative atomic distances. A pair additive sum over atomic distances is often assumed for the analytic function, leading to the total energy expression

$$\mathrm{E_{tot}} = \sum_i \sum_{(j\neq i)} \theta(r_{ij}) + \sum_k \varepsilon_k \tag{8}$$

where r_{ij} is the scalar distance between atoms i and j, θ(r) is a pair-additive analytic interatomic interaction, and ε_k are the energies of a set of occupied electronic orbitals. The simplest and most widespread tight-binding expressions use eigenenergies obtained from parameterized on-site and two-center hopping matrix elements assumed to be from a wavefunction expanded in an orthonormal minimal basis of short-range atom-centered orbitals.

The use of non-self-consistent one-electron molecular orbitals in tight-binding expressions is justified if the orbitals correspond to Kohn-Sham orbitals constructed from the input charge density in the Harris functional. Similarly, the analytic function in tight-binding total energy expressions can be justified if they correspond to the double counting terms constructed from the input charge density. [Foulkes (1989)]

The analytic bonding expression Eq.(2) can be derived from the tight-binding expression Eq.(8) through the moments theorem that relates the moments of the distribution of the electronic local density of states from the tight-binding molecular orbitals to the local bonding topology of a given atom. [Sutton (1993)] Specifi-

cally, the theorem states that "*the nth moment of the local density of states on an atom i is determined by the sum of all paths between n neighboring atoms that start and end at atom i*". In the second moment approximation it is assumed that the electronic bonding energy from the valence electrons of a given atom is proportional to the square root of the second moment of the local density of states of that atom. Through the moments theorem this is simply the square root of the number of neighbors of the atom. This relationship can be expressed analytically as

$$\mathrm{E}_i^{\mathrm{el}} = -\mathrm{A}\left[\sum_{(j\neq i)} e^{-\beta r_{ij}}\right]^{\frac{1}{2}} \tag{9}$$

where A and β are parameters that determine the contribution of surrounding atoms to the local bonding environment of atom *i*, and r_{ij} is the scalar distance between atoms *i* and *j*. With some straight forward algebra,[Brenner (1989)] Eq.(9) can be rearranged to an expression similar to Eq.(2) in which the bond-order function from atom *i* to atom *j* is

$$\mathrm{b}_{ij} = \left[1+\sum_{k\neq i} e^{-\beta(r_{ik}-r_{ij})}\right]^{-\frac{1}{2}} \tag{10}$$

and the two-center term is

$$\mathrm{V}^{\mathrm{A}}(r) \;=\; \mathrm{B}\, e^{-(\beta/2)r} \tag{11}$$

For regular structures (i.e. r_{ik}= r_{ij}) and considering only nearest neighbors the bond-order is proportional to the inverse square root of the local coordination as mentioned above. Substituting an angular function into the bond-order expression, and adding terms that account for radical energies and conjugation produces the empirical bond-order expression discussed above.

2.2 Self-consistent Environment Dependent Tight-Binding Method

The self-consistent tight-binding expression used below is essentially a modification to Eqs.(5) and (7). As discussed above, the Foulkes and Haydock interpretation of tight-binding theory is that the parameterized matrix elements used to obtain the non-self-consistent orbital eigenenergies correspond to Eq.(6) calculated from some assumed input charge density. In the self-consistent version of tight-binding theory, a perturbation to the input electron density is included, leading to matrix elements of the form

$$\hat{H} = -\frac{\nabla^2}{2} + V_{ext} + \int\left[\frac{\rho^{\mathrm{ref}}(R)}{|r-R|} + \frac{\Delta\rho(R)}{|r-R|}\right]dr + V_{xc}\left[\rho^{\mathrm{ref}}(R)\right] + \Delta V_x \tag{12}$$

Here Δρ is the difference between the actual electron density and some reference electron density ρ^{ref} to which the tight-binding parameters correspond

$$\Delta\rho = \rho - \rho^{\mathrm{ref}} \tag{13}$$

$\Delta \mathrm{V}_x$is the exchange potential associated with the electron density perturbation, and remaining terms are as described above. The term V_{ext} includes a Coulomb potential from both the atomic nuclei and any external fields, and is the term through which applied fields are included in the method.

Details regarding the form of Eq.(12), including the parameterization and fitting procedure, used in the calculations described below are given elsewhere.[Areshkin (2002)] The discussion is therefore limited to a general description of the approach. To make the calculations computationally tractable, a number of approximations are made. First, an orthogonal minimal Gaussian basis for the valence electrons is assumed, only the exchange portion of the exchange-correlation energy is included, and ΔV_x is approximated by its linear expansion with respect to Δρ at $\rho = \rho^{\mathrm{ref}}$. These approximations lead to analytic integrals that can be rapidly evaluated. Second, environment dependent on-site and hopping matrix elements introduced by Wang, Ho and co-workers for carbon are used to describe the terms involving the reference electron density in Eq.(12).[Tang (1996)] These are two-center terms with values that depend on the local bonding environments of the pair of atoms between which individual matrix elements correspond. This tight-binding approach is a computationally efficient scheme that eliminates some of the drawbacks associated with neglecting

orbital overlap terms without having to introduce a non-orthogonal basis. Finally, the diamond structure is used as the reference electron density. With this choice, the band structure of diamond, which was fit in the Tang parameterization, is maintained exactly, and changes to other band structures that entered the fitting procedure for the tight-binding parameters are not significantly altered by the electron density perturbation.

The Gaussian basis, together with carbon-hydrogen matrix elements arising from the reference electron density, was adjusted to fit electronic energy levels (with appropriate energy shifts) and Mulliken populations for several small hydrocarbon molecules and hydrogenated diamond nanoclusters as predicted from full density functional calculations. The resulting method describes a number of properties of hydrocarbon systems reasonably well. There are several shortcomings to the predictions of the method, however. Most notably, the polarizability of small molecules and the electron affinity of diamond are both underestimated. The former is due primarily to the orthogonal basis set, leading to a generally decreasing error as system size increases

As a final step to make the calculations computationally tractable, a modification to the Newton-Raphson method was developed that assures convergence even for starting configurations far from the final solution, and that produces solutions for metallic systems with reasonable scaling with the number of atoms.[Areshkin (2002)] This scheme, together with the approximations in basis set and energy functional, allows a self-consistent solution of the electronic states of hydrocarbon systems containing up to about a thousand atoms with very modest computing resources (e.g. a PC).

The two modeling methods described above, while having a common fundamental basis in density functional theory, are used for different situations. For cases where electronic structure is not needed, the bond order potential gives reasonably accurate energies and structures, and can model chemical reactivity in the form of bond breaking and forming for relatively large systems. For example, 100,000 atom systems can be routinely modeled on Intel-based PCs. The tight binding scheme is useful for situations where an estimate of electronic structure or electro-static properties of carbon-based systems are needed. The computational demands of the method currently place a practical limit of about two orders of magnitude fewer atoms than can be modeled with the bond order potential.

3 Survey of Systems and Results

Presented in this section is a survey of some recent applications of the modeling methods described in the previous section to carbon nanostructures. Some of the work discussed below was carried out with collaborators who are not listed as co-authors of the current paper. These collaborators are listed in the acknowledgements at the end of this paper. Much of the detail of the studies discussed below has been left out. More in-depth information is available in the original references.

3.1 New Materials and Devices from Nanotubes

The current interest in fullerene nanotubes was created when Iijima first reported observing these structures at the negative electrode of a carbon arc in a reactor designed to create fullerenes.[Iijima (1991)] The production and processing of these structures has advanced to the stage where fullerene nanotubes can now be created as both single and multi-walled structures by a number of different processes in relatively large quantities. This has created a great deal of interest in using them for a number of applications, including in structural and thermal management materials, as energy storage media, cold cathodes for flat-panel displays, and components of nanoelectronic devices.

Nanotubes can be envisioned as rolled-up graphite planes (although they are not created that way), and are found both as single and multi-walled structures, with either open or capped ends.[Dresselhaus (1996)] The structure of a nanotube of infinite length can be conveniently denoted by (n,m), where n and m refer to the contribution of the two primitive in-plane lattice vectors of graphite to the vector defining the circumference of the nanotube. The highest symmetry structures, for which the vector describing the circumference of the nanotube is perpendicular to the nanotube axis, are the (n,n), or armchair structure, and the (n,0), or zigzag structure. Taking the boundary conditions associated with the circumference of nanotubes into account, simple tight-binding theory predicts that if

$$2n+m=3q \tag{14}$$

is satisfied where q is an integer, the nanotube will not have a band gap. If Eq.(14) is not satisfied, tight-binding

theory predicts that a nanotube will be semiconducting. For all nanotubes except the armchair structure, however, the occupied and unoccupied energy states are degenerate at the Fermi level at the gamma point, and more sophisticated calculations predict a loss of this degeneracy and a small band gap. The (n,n) nanotubes, on the other hand, have a curve crossing at the Fermi level, and are all therefore predicted to be metallic. The magnitude of the band gap of semiconducting nanotubes is also predicted to depend on the nanotube radius.[White (1993)]

3.1.1 Properties of Functionalized Nanotubes

Many of the mechanical and electrical properties of pristine nanotubes have been reasonably well characterized by theory and modeling. The relationship between band gap and structure, for example, has been established, and significant progress has been made in understanding the transport properties of nanotubes.[Bernholc (2002)] The elastic modulus of nanotubes, the formation of kinks due to severe mechanical distortion, and plastic deformation mechanisms have been modeled both from an atomic and continuum viewpoint. In contrast, the properties of nanotubes whose sidewalls have been functionalized have not been as well studied as pristine nanotubes. Exceptions are the work of Sinnott and co-workers, who examined the changes in the compressive force needed to create kinks in nanotubes functionalized with H_2C=C species[Garg (1998)], and Frauenheim and co-workers, who studied changes in electronic properties with sidwall fluorination.[Seifert (2000)] The primary reason that the properties of sidewall functionalized nanotubes have not yet been well characterized is that the experimental ability to chemically add species to sites other than the caps of nanotubes is a recent development. Functionalization, however, may lead to optimized and new technology applications of nanotubes, including increasing load transfer in polymer-nanotube composites, and tuning the band gap of nanotubes for nanometer-scale electronic device applications as discussed below.

Using the bond-order potential above, the tensile modulus of several nanotubes whose sidewalls have been functionalized with different densities of methyl radicals was theoretically explored. The chief motivation for this work comes from the nanocomposites, where cross-linking a nanotube into a polymer matrix may be a viable method to enhance load transfer between a nanotube fiber and matrix.[Frankland (2002)] This is discussed in more detail below. However, functionalization will rehybridize any carbon atom in a nanotube to which a sigma bond is formed. This has the potential to reduce the tensile modulus of a nanotube, although the fraction of sites that need to be rehybridized to induce a significant reduction is not clear.

Illustrated in Fig. 1 is a section of a (17,0) nanotube to which a methyl radical has been chemically attached. The atomic positions were obtained by minimizing the energy given by the bond-order potential discussed above. As expected, formation of the sigma bond causes the bond angles of the carbon atom in the nanotube to which the methyl is attached to approach the tetrahedral angle. To help determine the extent to which chemical functionalization could reduce the tensile modulus of a nanotube, systems were generated in which methyl radicals were added to (10,10) and (17,0) nanotubes at different chemisorption densities up to 15% of all carbon sites. The sites for chemisorption were chosen randomly, and the energies of the systems were minimized using the bond-order potential. Illustrated in Fig. 2 is the configuration for 15% chemisorption to a (17,0) nanotube. Plotted in Fig. 3 is the energy as a function of strain for both pristine and 15% functionalized (10,10) and (17,0) nanotubes. These were generated for infinite systems under one-dimensional periodic boundary conditions by straining the periodic boundary in small increments, and then minimizing the energy given by the bond-order potential. Interestingly, there is little difference between the functionalized and pristine curves for the (10,10) nanotube, while functionalization has reduced the modulus of the (17,0) nanotube to that of the pristine (10,10) nanotube. In both cases, however, even this relatively large functionalization density does not appear to significantly decrease the tensile modulus.

Plotted in Fig.4 is the minimum energy strain of a functionalized (10,10) nanotube relative to the pristine system as a function of the fraction of sites to which methyl radicals are added. To obtain these curves, the energies of the nanotubes were minimized both with respect to the atomic configurations and the length of the periodic cell in which the nanotube is embedded using the bond-order potential. These simulations predict that the entire nanotube contracts slightly with increasing degree of functionalization.

Tight-binding calculations have also suggested that the band gap of a nanotube can be altered via functional-

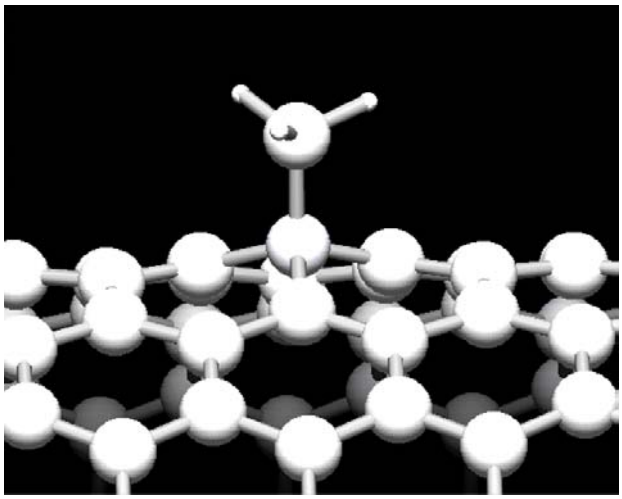

Figure 1 : Section of a (17,0) nanotube to which a methyl radical has been chemically attached.

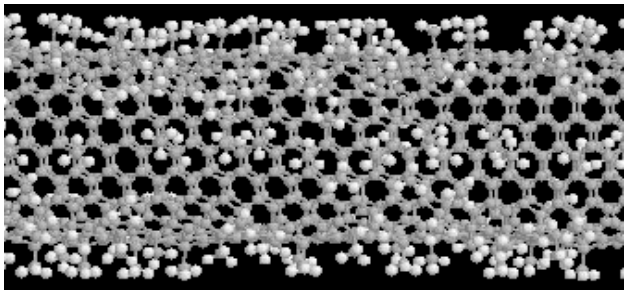

Figure 2 : Illustration of a (17,0) nanotube on which methyl radicals have been chemisorbed to 15% of the nanotube carbon atoms.

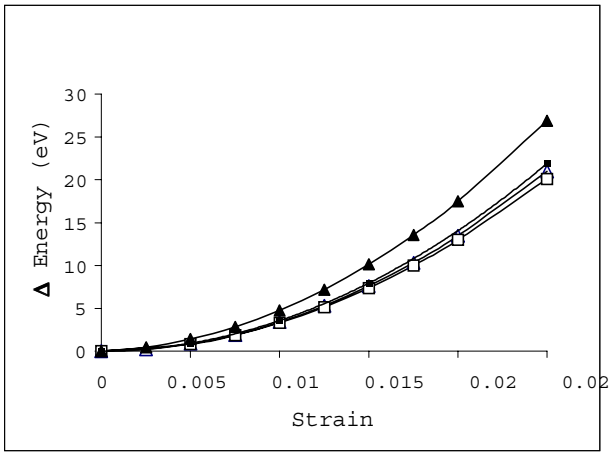

Figure 3 : Potential energy as a function of strain for both pristine (triangles) and 15% functionalized (squares) (10,10) and (17,0) nanotubes (open and closed symbols, respectively)

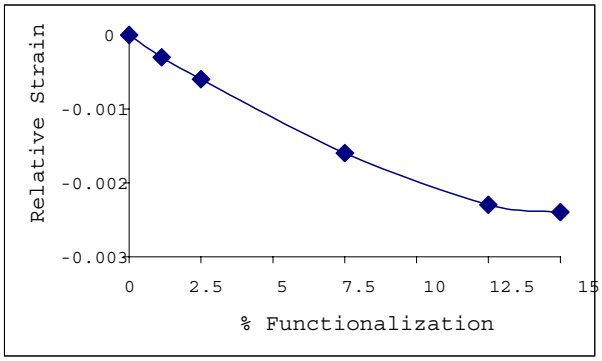

Figure 4 : Minimum energy strain of a functionalized (10,10) nanotube relative to the pristine system as a function of the fraction of sites to which methly radicals are added.

ization. [Brenner (1998b)] This result suggests that the electronic properties of a nanotube could be altered along its length by functionalizing finite regions of a nanotube, leading to, for example, metal-semiconductor junctions and quantum dots along the length of a single nanotube. Two levels of tight-binding calculation were performed. In the first, only the pi system was considered, and matrix elements between nearest neighbors were used to representing overlap of p orbitals contributing to the pi system. The model assumes that the formation of a sigma bond to an atom removes the atom from the pi system and creates a node in the pi wave functions. This can alter the allowed energy states, and if the states are near the Fermi level a band gap can be introduced to a metallic system or removed from a semiconducting system. To model the node, the hopping matrix elements between that atom and its neighbors are set to zero.

For certain high-symmetry chemisorption sites, the simple tight-binding model leads to qualitative predictions for the presence or absence of a band gap. For example, chemisorbing species with two bonds across a six-membered ring on an (m,0) nanotube such that a set of binding sites are created perpendicular to the nanotube axis in each translational unit cell effectively breaks the pi system into independent regions. This is illustrated in the middle and bottom panels of Fig.5 for a (6,0) nanotube. In this case, the nodes in the pi wavefunctions retain the same symmetry as the azimuthal boundary conditions of the pristine nanotube; however, wavefunctions must have one-half wavelengths (rather than whole wave-

lengths) that fit within these regions. From this relation it can be shown that regions with widths of L lattice units will not have a band gap when

$$2L/3 = q \tag{15}$$

is satisfied, where q is an integer. The middle of Fig.(5) illustrates the case in which chemisorption produces two regions of width L=3. According to Eq.(15), these regions will be metallic. In contrast, the bottom of Fig.5 illustrates the case in which regions of L=4 and L=2 are produced. The model predicts that both regions will have a band gap, and therefore chemisorption at these sites are predicted to alter the electronic properties of a (6,0) nanotube from metallic to semiconducting. Similarly, (n,0) nanotubes, where n is not a factor of three, can be made metallic by producing one or more regions via chemisorption with widths that satisfy Eq.(15).

The second tight-binding model uses a minimum basis of one s and three p atomic orbitals for each valence electron. Hopping and overlap matrix elements were used that were fit by White and coworkers to polymer properties and fullerene band gaps.[Elert (1985)] Systems were generated that correspond to those illustrated in Fig. 5 at the minimum energy configurations predicted by the bond-order potential. Periodic boundaries were used along the length of the nanotube, and a sufficient number of k points were used to obtain a converged density of states. Plotted in Fig. 6 are the density of states in the vicinity of the Fermi level calculated for a pristine (6,0) nanotube and one on which ethene molecules are chemisorbed at the sites indicated at the bottom of Fig. 5. The model predicts that chemical addition of the ethene molecules at these positions opens a band gap of 1.3 eV in this nanotube, in agreement with the qualitative predictions of the simpler tight-binding model.

Illustrated in Fig.(7) is a region of a (6,0) nanotube on which ethene molecules have been chemisorbed along one-half of a nanotube length at the sites illustrated at the bottom of Fig.(5). The structure of the system was again obtained by minimizing the energy given by the bond-order potential energy function. According to the tight-binding calculations on the pristine and fully chemisorbed systems, this structure is essentially a metal-semiconductor junction with a Schottky barrier of 0.44eV. For comparison, silicon has a band gap of 1.1 eV and a Si-Al interface has a Schottky barrier of 0.6eV.[Louie (1977)] Plotted in Fig. (8) are local densities of states averaged over the first and second translational unit cells, respectively, away from the junction into the chemisorbed region of the nanotube. There are metal-induced gap states that decay in magnitude

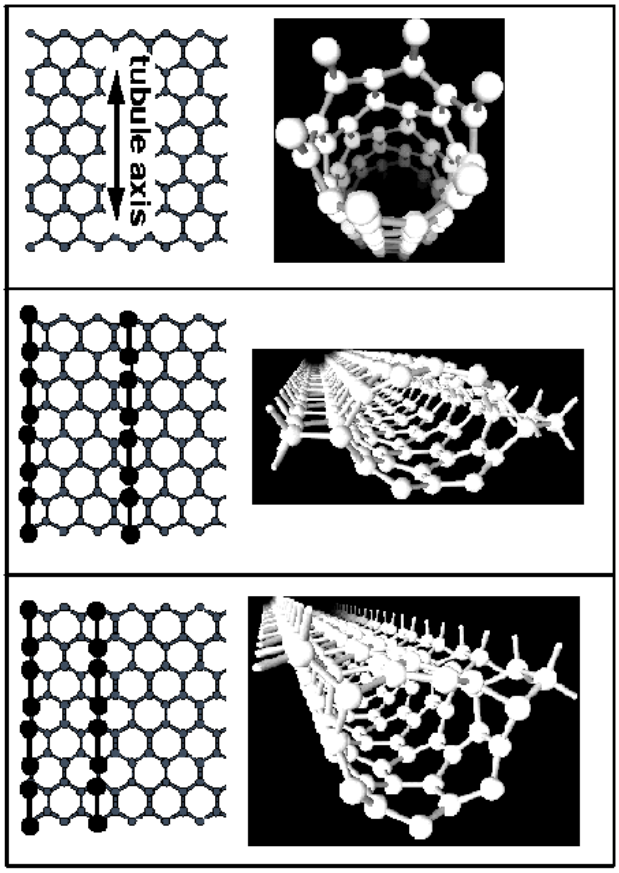

Figure 5 : Illustration of regions of pi bonding created by chemisorption to a (6,0) nanotube. Top: Pristine nanotubes. Middle: Chemisorption creating two regions three lattice units wide. Bottom: Chemisorption creating regions two and four lattice units wide.

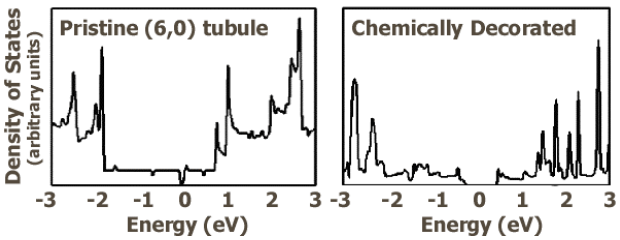

Figure 6 : Density of states in the vicinity of the Fermi level for a pristine (6,0) nanotube and one on which ethene molecules are chemisorbed at the sites indicated at the bottom of Fig. 5.

away from the junction. Similar states have been characterized with first-principles methods for more conventional metal-semiconductor junctions, including Si-Al and GaAs-Al interfaces.[Louie (1977)] To characterize the decay length, the local density of states for each unit cell near the junction was integrated over the states in the band gap of the functionalized structure. The value of the integral as a function of unit cell position is plotted in Fig.(9). Fitting the decay of these states into the semiconducting region to an exponential function yields an attenuation length of 4.5A, a value that is comparable to that of a Si-Al interface. [Louie (1977)]

3.1.2 Chemical Reactivity at Kinks

The modeling methods described above were used to explore whether kinks and other regions of high curvature induced by mechanically deforming nanotubes can act as sites of enhanced chemical reactivity.[Srivastava (1999)] In these calculations, single-walled (17,0) and (10,10) nanotubes were bent or twisted, and the resulting structures obtained by minimizing the energy as given by the bond-order function. The binding energies for chemisorbing single hydrogen atoms to the distorted nanotubes were used as a measure of the relative chemical reactivity at different nanotube sites. Illustrated in Fig.(10), for example, is the predicted atomic structure near two kinks formed in a bent (17,0) nanotube as viewed from the back of the kinks. The nanotube flattens along the front and back of the kink where the system is under compressive and tensile hydrostatic stress, respectively. Between these two regions there is a "ridge" of atoms along the kink top and bottom. This is essentially the same structure that would be obtained if a typical garden hose were bent enough to kink. This ridge is raised at the center of the kink, and the angles of the three bonds associated with the atom of the ridge apex are close to tetrahedral.

The bond-order potential predicts that a hydrogen atom is more strongly bound to the apex carbon atom along the ridge by about 1.6 eV relative to chemisorption at an undistorted region of the nanotube. The binding energy enhancement drops off smoothly for the carbon atoms along the top of the ridge, dropping to an enhancement of 0.25eV for the sites five atoms from the apex (Fig.(11)). This increase in binding energy at the kink correlates with a decrease in atomic cohesive energy as predicted both from the analytic force expression and from non-

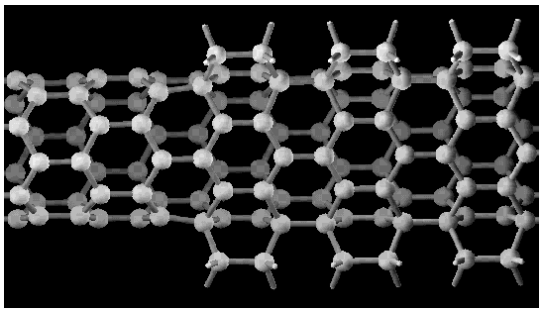

Figure 7 : Illustration of a (6,0) nanotube on which ethene molecules have been chemisorbed along one-half of the nanotube length at the sites illustrated at the bottom of Fig. 5.

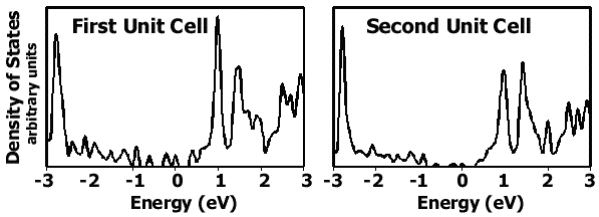

Figure 8 : Local density of states averaged over the first (left) and second (right) translational unit cells, respectively, away from the junction into the chemisorbed region of the nanotube.

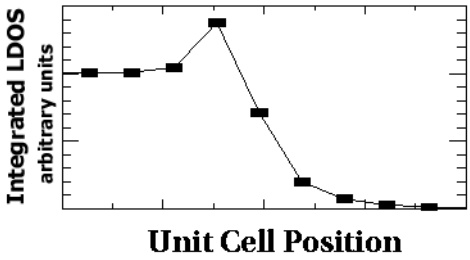

Figure 9 : Value of the local density of states integrated for each translational unit cell over the energies corresponding to the band gap of the functionalized region of the nanotube as a function of the position of the unit cell.

self-consistent tight-binding calculations.

Hydrogen atom binding was found to be weaker relative to an undistorted nanotube for sites along the back and front of the kink. At the back of the kink, the nanotube is under tensile hydrostatic stress, and subsequently the tetrahedral bond angles required for strong chemisorp-

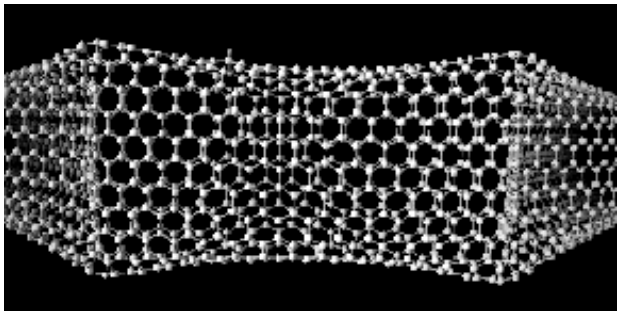

Figure 10 : Illustration of kinks formed in a bent (10,10) nanotube.

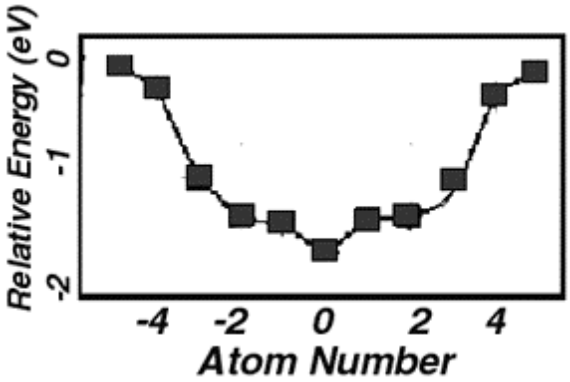

Figure 11 : Hydrogen binding energy relative to a single hydrogen atom and a pristine nanotube for sites along the top of the ridge of atoms formed at the kink.

tion are more difficult to form compared to an undeformed nanotube. At the inside of the kink, the nanotube structure is deformed such that carbon atoms are distorted toward the interior of the nanotube, leading to an improper geometry for strongly binding hydrogen atoms to the outside of the nanotube.

A similar enhancement in hydrogen binding energy was predicted for chemisorption along ridges formed from twisting a nanotube.[Srivastava (1999)] In addition to the energy calculations, classical trajectories were carried out in which atomic hydrogen was allowed to react with the twisted nanotube. Consistent with an increase in binding energy, the trajectories predicted enhanced sticking of the hydrogen to the ridges.

Enhanced chemical reactivity at regions of large nonlinear distortion on nanotubes as inferred from the simulations has been supported by experimental observations by Ruoff and co-workers.[Srivastava (1999)] In these experiments, multi-walled nanotubes were placed along a polymer substrate containing V-shaped ridges, and dilute nitric acid was introduced into the system. Scanning electron microscopy showed significant nanotube etching where the nanotubes were draped along the substrate ridges where presumably the high curvature induced kinks in the nanotubes. While indirect proof, the observation of enhanced etch rates supports the connection between enhanced chemical reactivity and large distortions of nanotubes predicted by the calculations.

3.1.3 Nanocones

Using the atomic simulation methods discussed above, the structure and electronic properties of nanocones as well as the possibility of assembly these species to more extended structures were studied.[Shenderova (2001)] Pentagonal or heptagonal defects can be introduced into graphene networks to form nonplanar structures. An example are nanocones, structures with five-fold symmetry that cap nanotubes and that have been found as free standing structures formed in a carbon arc. The observed structures normally have opening angles of $\sim 19^o$ due to the introduction of one pentagon into the hexagonal network, and can be as long as $\sim$240 Å.[Dresselhaus (1999)]

Carbon nanocones are geometrically similar to diamond pentaparticles, structures that have been observed experimentally as free-standing structures and as fivefold microcrystals embedded in chemical vapor deposited diamond films. In the simulations, pentagonal diamond crystals were used to generate graphite cones by ”lifting off” atomic layers, and allowing the resulting structures to relax to their minimum energy configuration as given by the bond-order potential. When pentagonal crystals with radii less then 14 Å were used to generate carbon cones, the systems relaxed to a conventional cone shape such as that illustrated in Fig 12. However, for larger radii particles alternate metastable structures formed during system relaxation. These structures, which posses low symmetry ‘wave’-like shapes (Fig.13) are formed because of an increase in excess strain energy due to the larger radius that creates a larger initial system instability. Annealing beyond 300K via molecular dynamics simulations results in the conversion of the cones to the lower energy structure.

The simulations predicted that it is also possible to change the shape of a conventional cone by ’pushing’ the cone from the top with an indenter. Furthermore,

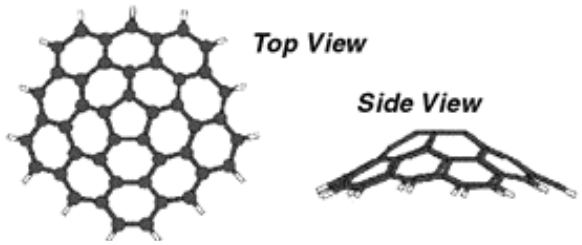

Figure 12 : Illustration of a fullerene nanocone.

'waved' structures were observed that have several rings of compressive and tensile hydrostatic stresses that alternate along the cone radius. Therefore modeling indicates that depending on radius, nanocones may exhibit several metastable structures, with transformations between these structures depending on external conditions. This environment-dependent reversible-shape transformation result suggests shape could potentially be used as a means of information storage.

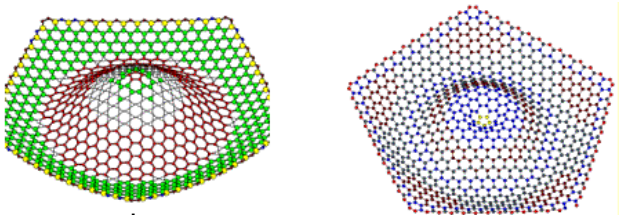

Figure 13 : Illustration of distorted nanocones.

Structures and stresses associated with assemblies of nanocones were also modeled. Nanocones can be connected to form extended structures by forming chemical bonds between cones along their edges. For example, self-similar structures with five-fold symmetry can be generated that can contain a high density of nanocones (Fig. 14). The assembly of such structures can result in wide variety of patterns whose buckling depends on the number of cones, the hydrogenation of any dangling bonds, and in the convex or concave structures of the nanocones.[Shenderova (2001)]

3.1.4 Polymer-Nanotube Composites

Their high thermal conductivity and large tensile modulus, together with the ability to bridge and heal cracks,[Ajayan (2000)] have made nanotubes target components of light-weight, nanoscale fiber-reinforced composites for mechanical and thermal management applications. Reports of measured enhancements in the elastic modulus of polymers with the addition of a few percent nanotubes[Andrews (1999); Qian (2000)] together with apparent Raman frequency shifts for nanotubes in loaded polymer matrices [Wood (2000); Ajayan (2000); Hadjiev (2001); Zhao (2001)] suggest that load transfer from the matrix to the nanofibers can be strong enough to use these systems for structural applications.

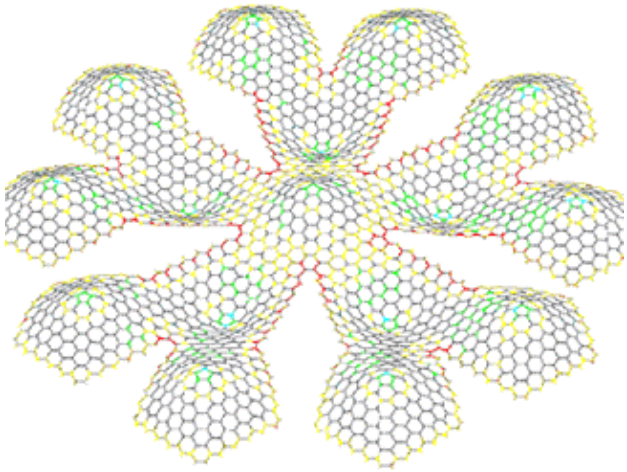

Figure 14 : Illustration of a self-similar structures with five-fold symmetry generated from a high density of nanocones.

Specific mechanism(s) by which load is transferred between polymer matrices and nanotubes is not clear. Determining this mechanism (and ways to enhance it) has been a central focus of recent molecular modeling studies. Lordi and Yao used force-field-based molecular mechanics to model the interactions between nanotubes and several polymers.[Lordi (2000)] The authors suggest that helical polymer conformations in which chains wrap around nanotubes might produce strong nanotube-polymer interactions.

In related studies, molecular simulations were used to estimate shear strengths and critical fiber lengths for efficient load transfer for several models of a polyethylene-nanotube composite, including a composite with a low-density of cross-links between the nanotube and the matrix.[Frankland (2002)] This matrix-fiber system was chosen because of its simplicity, and not because it would make a composite with particularly strong interfacial interactions, or is experimentally accessible. It is a convenient system for which the nanotubes, matrix, and any chemical bonding between these can be consistently

modeled with a hydrocarbon potential.

The nanotubes and their chemical cross-links to the polymer were modeled by the bond-order potential described above. To study the influence of the details of the matrix structure as well as that of the matrix-nanotube interface on possible load transfer, several matrix structural and bonding models were used. These included crystalline and amorphous matrix structures, as well as both a model that explicitly includes hydrogen atoms and an "united atom" approximation in which hydrogen atoms and the carbon atoms to which they are bonded are treated as a single unit. In each case the nonbonded polymer-nanotube and the polymer-polymer interactions were modeled with pair additive Lennard-Jones potentials. Intramolecular interactions within the polymer chains were either modeled with appropriate combinations of valence force bond stretch and bend terms, or the bond-order potential used to model the nanotubes.

In initial studies, molecular dynamics simulations were used to model loading strain for composites containing (10,10) nanotubes in which only weak nonbonded interactions between the nanotubes and matrix were included. In the case of nanotubes of infinite length created via periodic boundary conditions, an enhancement in modulus consistent with a simple rule of mixtures was obtained. Similar simulations were also carried out in which capped nanotubes of finite lengths embedded in the various matrix models were simulated. The largest system contained a 100 nm long nanotube in a united-atom/amorphous polyethylene matrix. In each of these loading simulations the nanotubes released from the matrix starting at their ends and regained their initial length, indicating negligible load transfer for these systems.

To further quantify critical fiber lengths needed for good load transfer, a series of virtual fiber "pull-through" simulations were carried out. In these studies, infinite nanotube-polymer systems were created via periodic boundaries, and a one-body force of increasing magnitude was applied to the nanotube until the nanotube began to move relative to the matrix. This force divided by the estimated contact area between the nanotube and matrix was then taken as the shear strength τ_c. This value can be combined with the nanotube diameter d and tensile strength $\sigma_f$go estimate the minimum length l_c need for efficient load transfer through the expression

$$l_c = \sigma_f d/\tau_c \tag{16}$$

Given in Tab. 2 are shear strengths and critical fiber lengths for several matrix models estimated from these simulations. For strictly nonbonded interactions, the fiber-matrix shear strengths ranged from 2.7 MPa for the amorphous matrix/united atom potentials to 2.8 MPa for the crystalline matrix/explicit hydrogen model. Assuming a fiber strength of 50 GPa for the nanotubes,[Yu (2000)] these shear strength values imply that lengths exceeding about 25 microns would be needed for significant load transfer between the matrix and nanotube. These lengths and shear strengths are consistent with the lack of load transfer observed in the molecular dynamics simulations of loaded systems mentioned above. Worthy of note from this data is that the chemical details of the polymer model (i.e. explicit vs. united atom models) apparently govern the estimated shear strengths and the critical fiber lengths much more than does the matrix structure model (i.e. crystalline vs. amorphous). This result is despite the difference in density between the amorphous (0.71 g/cm^3) and crystalline (0.94 g/cm^3) matrices used in the simulations.

Table 2 : Shear yield strengths for nanotube-matrix interfaces and corresponding minimum nanotube lengths needed for efficient load transfer.

System	***Fiber-Matrix Shear Strength (MPa)***	***Minimum nanotube length (microns)***
Non-bonded/no cross-links		
Amorphous	2.7	30
Crystalline	2.8	29
Cross-linked Systems		
Amorphous	2.0/30.0	40/2.6
Crystalline	6.8/110	11.7/0.72

The influence of chemical cross-links between a single-walled fullerene nanotube and a polymer matrix on the matrix-nanotube shear strength and critical length for load transfer was also studied using molecular dynamics simulations. The motivation for these studies came from two sources. First, it is desirable to establish in a general sense whether a sufficiently small density of cross-links can be created that enhance load transfer while not compromising the tensile moduli of single-walled nanotubes. Second, it has been suggested that chemical interactions between nanotubes and a matrix created dur-

ing processing may be responsible for the stress transfer value of 500 MPa estimated in epoxy/nanotube composites.[Wagner (1998)] The modeling studies discussed here begin to establish whether such a large stress transfer is possible in these types of nanocomposite systems via chemical bonding between the nanotubes and matrix.

A (10,10) nanotube 53A in length containing 880 atoms was embedded into the crystalline matrix, and a total of 6 ethylene oligomer cross-link chains containing 12 monomers were created between the nanotube and matrix (Fig. 15). This system therefore has a grafting density relative to the nanotube atoms of less than 1%. To treat the nanotube, ethylene matrix and cross links on an equal footing, the bond-order potential was used for all intramolecular interactions, while the intermolecular interactions were modeled with the same Lennard-Jones potentials as was used in the other explicit-hydrogen matrix models. A similar system was created for the amorphous matrix, although at a lower grafting density (0.3%).

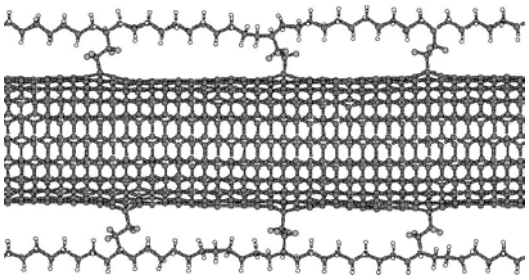

Figure 15 : Illustration of a (10,10) nanotube cross-linked into a polyethylene matrix.

Two distinct processes were observed in the virtual pull-through studies with the cross-linked systems, and therefore two sets of τ_c values are reported in Tab. 2. The lower values of τ_c correspond to the applied stress at which the nanotube alone first begins to shear with respect to the matrix. The higher value of τ_c denotes the force at which the nanotube initially pulls one or more polyethylene chains with it through the matrix. The crystalline composite has an initial τ_c that is larger by about a factor of two over the corresponding system with only nonbonded interactions, while for the amorphous composite the lower value of τ_c is comparable to the nonbonded systems. This result indicates that the initial yielding in the crystalline system may be reinforced, albeit by a relatively small amount. In both the crystalline and amorphous matrix models the shear strength required to begin pulling the chains through the matrix is about 15 times that needed to start the initial motion of the nanotube, resulting in a significant shortening of the critical fiber needed for good load transfer. This result, together with the prediction of the mechanical properties of functionalized nanotubes mentioned above, suggests that chemical functionalization leading to matrix-nanotube cross-linking may be an effective mode for enhancing load transfer in these systems without sacrificing the elastic moduli of nanotubes.

3.1.5 Raman Shifts of H_2 in Nanotubes

Fullerene nanotubes have been targeted as hydrogen storage media for a number of applications, including rocket propellants and vehicular fuel cells, where they may provide a safe alternative to compressed or liquefied fuels. The amount of hydrogen that can be stored in nanotubes, however, has been somewhat controversial. For "pure samples", reported experimental values for weight percent hydrogen uptake range from 0.4% to as high as 10% ($\sim$50 kg/m^3) depending on the temperature and pressure.[Dillon (1997); Nutzenadel (1999); Ye (1999)] The higher range of uptake measurements are close to target values of 6.5 wt% and 62 kg/m^{3}recommended by the Department of Energy Hydrogen Plan, suggesting that nanotubes can make effective hydrogen storage media if the higher range of experimental values are accurate.[Hynek (1997)] One of the highest reported hydrogen uptakes is 14 wt% and 112 kg/m^{3}observed at 313 K for the catalytic storage of hydrogen in potassium-doped nanotubes.[Chen (1999)]

The authors of one of the experimental studies have noted that their values of $\sim$5-10 wt% hydrogen uptake in pure nanotube samples exceeds the amount predicted by a simple analysis of packing molecular hydrogen inside a nanotube, and they have therefore proposed both external and interstitial adsorption. Computational studies have supported this conclusion, where amounts for hydrogen storage within nanotubes that are lower than the experimental values are typically reported for ambient conditions. [Wang (1999); Simonyan (1999); Darkrim (1998)]

Based on experimental and computational studies, a key issue related to hydrogen storage by nanotubes is the location of the hydrogen, i.e. is hydrogen primarily stored inside nanotubes, between nanotubes, or both? One technique that could potentially shed light on this issue is

Raman spectroscopy. In this method infrared adsorption associated with the excitation of Raman active vibrational modes is measured. Due to anharmonicities in intramolecular potentials, the average size of a diatomic molecule (like hydrogen) is generally larger in an excited vibrational state relative to the ground vibrational state (for the same electronic state). In confined environments, the energy of a molecule will depend on its size and shape relative to that of its environment. This implies that the energies of different vibrational states of a molecule will depend on the relative "sizes" of the vibrational states and on the confining environment. Because in Raman spectroscopy energy differences between vibrational states are measured, the Raman adsorption frequency will depend on the local environment of the adsorbing molecule. This value is usually reported as a frequency shift relative to an isolated molecule. It is expected that a Raman shift measured for a hydrogen molecule intercalated into nanotubes will depend on the environment, i.e. on whether a hydrogen molecule is adsorbed inside of or between nanotubes. However, the relationship between the magnitude and sign (i.e. blue or red) of a Raman shift and the hydrogen environment in nanotubes is not *a priori* known, and therefore some guidance from theory is needed to interpret any such shifts.

To help determine the dependence of Raman shift on intercalation environment for hydrogen in nanotubes, a semiclassical model was used to predict qualitative trends in Raman shifts relative to the gas-phase vibrational frequency for a single hydrogen molecule within and between bundled nanotubes of various radii.[Frankland (2002)] The model uses classical trajectories to sample the surroundings of a hydrogen molecule in the different environments. Relative Raman shifts are estimated from the energy difference averaged over a trajectory in each environment between the ground and first excited vibrational state of the hydrogen molecule. The bond-order potential discussed above was used to model intramolecular forces within the nanotubes, and appropriate Lennard-Jones interactions were used to model inter-nanotube forces. The hydrogen molecule was treated as a rigid rotor, and the motion of the molecule was calculated by integrating classical equations of motion using Lennard-Jones forces between the hydrogen and carbon atoms that are appropriate for the ground vibrational state of hydrogen. During the trajectories on the ground-state potential, energies were calculated from a second set of Lennard-Jones carbon-hydrogen interactions with parameters that reflect changes in average hydrogen-hydrogen bond length and molecular polarizability for a molecule in the first excited vibrational state. The energy difference between the two sets of Lennard-Jones parameters for trajectories during which hydrogen samples either inside or in the region between nanotubes in a bundle provides a qualitative estimate for the Raman shift due to the different environments.

Three different hydrogen environments were simulated, each of which involved single-walled nanotubes of various radii and chiralities. These environments were a hydrogen molecule inside an individual nanotube, a molecule inside the center nanotube of a rope of 19 nanotubes, and a hydrogen molecule intercalated between nanotubes. In each of these systems, periodic boundaries were used along the nanotube axis, yielding nanotubes of infinite length. Plotted in Fig. 16 are predicted Raman shifts for a single hydrogen molecule inside various nanotubes as a function of nanotube radius. Results for both single nanotubes and nanotube bundles are plotted. Several trends are apparent from this data. First, the predicted shift does not depend strongly on the chirality of the nanotube in which the hydrogen molecule is placed or whether the nanotube is isolated or part of a bundle. Second, all of the Raman shifts are red indicating that the hydrogen is relatively free to vibrate without compression. Finally, there is an increase in Raman frequency with increasing nanotube radius up to a limiting value at a radius of about 20 Å. In the systems corresponding to the limiting Raman shift, the hydrogen molecule senses only one side of the nanotube during a trajectory. At the smallest nanotube radii simulated, the hydrogen interacts with both sides of the nanotube simultaneously, resulting in a Raman shift of roughly double that of the limiting value. The Raman shift changes continuously between these two limits.

Plotted in Fig. 17 are predicted average Raman shifts for hydrogen intercalated between nanotubes within a bundle as a function of nanotube radius. Each point represents an average over several starting configurations. Several trends are evident from this data. First, the magnitude of the shifts for intercalated hydrogen is generally larger than that for hydrogen inside of a nanotube. Second, the smaller ropes ($r<8$ Å) do not intercalate hydrogen well. Neither a (10,10) rope nor a (17,0) rope was

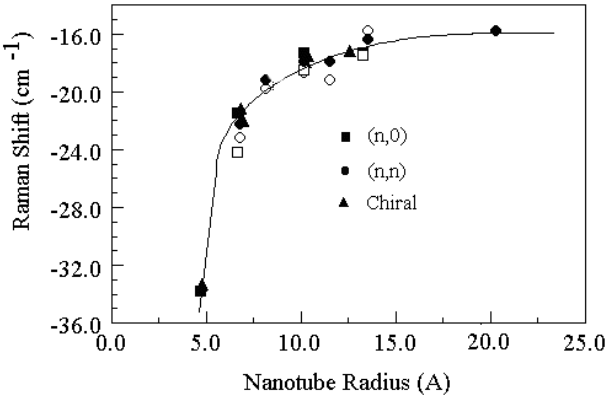

Figure 16 : Predicted Raman shifts for a single hydrogen molecule inside various single-walled nanotubes as a function of nanotube radius. Closed symbols - single nanotubes; Open symbols - nanotube ropes.

able to accommodate intercalated hydrogen. Third, when hydrogen can be intercalated, there is significant scatter in the average shift for trajectories in the same system but initiated with different starting conditions. Apparently there are different nanotube deformations that accommodate the intercalated hydrogen that persist longer than the 40 picoseconds over which the trajectories are run. Finally, for the (n,n) ropes there is no significant trend in shift with nanotube size. For the (n,0) ropes the data indicates that there may be a slight increase in peak frequency with nanotube size, although this increase is small compared to the internal hydrogen shift and would likely be obscured in an experiment by the broadening of the peak from several intercalation environments. It is therefore unlikely that shifts arising from intercalated hydrogen molecules will show a consistent trend with nanotube size.

The relationships between the location of a hydrogen molecule and its Raman shift predicted from these calculations can be summarized as follows. First, Raman shifts for individual hydrogen molecules are expected to be red-shifted independent of the site at which the hydrogen resides. Second, if the hydrogen is internal to the nanotubes, the Raman peak frequency is expected to show an increase with nanotube radius. If the hydrogen is intercalated, broader bands will be observed with no frequency dependence on the nanotube size. These frequencies will be lower on average than those from internal hydrogen. Third, it is energetically unlikely for ropes of very small nanotubes (r$<$8Å) to intercalate hydrogen. Finally, for very large nanotubes (r$>$20 Å), the Raman frequency is expected to be independent of nanotube size for either type of hydrogen. The cases examined here indicate that if both intercalated and internal hydrogen were present, the frequencies of the bands would be resolvable. To date, these predictions have not yet been verified (or refuted) by experiment, and the location of hydrogen adsorbed into samples containing nanotubes remains of interest both experimentally and theoretically.

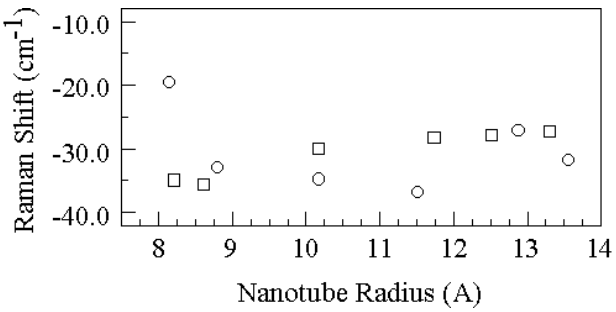

Figure 17 : Predicted average Raman shifts for hydrogen intercalated between nanotubes within a bundle as a function of nanotube radius.

3.1.6 Nanotribology on Graphite

Superfine and coworkers have experimentally observed interesting behavior for nanotubes manipulated on a graphite substrate. Using a nanomanipulator, it was observed that nanotubes initially slide about a pivot point relatively easily before locking into a position in which the nanotube and graphite lattices apparently line up.[Falvo (2000)] After 'locking-in', it was inferred from surface images of asymmetric nanotubes that nanotubes prefer to roll rather than slide while being pushed with an atomic-force microscope tip. The rolling motion itself, however, could not be imaged. In a related study, it was observed that current-voltage relations for electron transport between the graphite and a scanning-probe microscope tip through a nanotube depended on whether the nanotube was in or out of registry with the graphite.[Paulson (2000)] These electronic properties together with the sliding and rolling behavior suggested the potential construction of novel actuating devices from nanotube-graphite systems.

This interpretation of the experimental data that nanotubes that are out of registry with a graphite lattice slide while in-registry nanotubes prefer to roll was

tested using molecular dynamics and quasi-static simulations.[Buldum (1999); Schall (2000); Falvo (2002)] In the molecular dynamics simulations,[Schall (2000)] a single-shell (10,10) nanotube was placed on a graphite substrate (Fig. 18), while in the quasi-static calculations, a larger nanotube with a radius closer to that of the outer shell of the nested structures studied experimentally was modeled.[Buldum (1999)] In both simulations the nanotube-graphite interactions were modeled by a pair-additive Lennard-Jones potential. The chief difference between the two set of simulations was that in the molecular dynamics studies the nanotube and the first graphite layer was allowed to deform according to the bond-order potential described above. In the quasi-static simulations the relative atomic positions of the nested nanotubes were held fixed as the structure was moved across the substrate. Both sets of simulations confirmed an energetically preferred configuration in which the lattices of nanotubes and graphite are aligned. To study dynamic behavior in the molecular dynamics studies, nanotubes were placed either in or out of registry with respect to the graphite substrate. An impulse was applied to the nanotubes in turn, and the subsequent dynamics were followed as each nanotube moved. For the out of registry case, the nanotube slid along the surface, with frictional forces slowing the structure. When in registry, however, it was observed in the simulations that the nanotube initially slid, and then underwent an alternating rolling-sliding motion as it slowed down (Fig. 19). The net result is a rolling of the nanotube as it moves along the substrate, but with a complicated mechanism that could not be discerned from the experiments alone. An identical mechanism was independently identified from the quasi-static calculations. [Buldum (1999)]

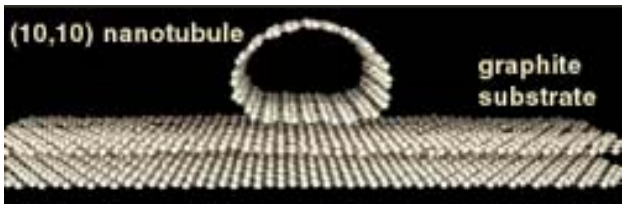

Figure 18 : Illustration of a single-shelled nanotube on graphite.

3.1.7 Nanotubes in Electric Fields: Dipole Moment and Polarization Energy

The properties of nanotubes in applied electric fields are of interest for a number of applications, including using nanotubes as electromechanical switches, field-emission sources, and nanoelectronic device elements. To help support the development of these technologies, calculations of some static properties of nanotubes in applied fields are being carried out using the self-consistent tight-binding scheme outlined above. Worthy of note is that this computational method can also be used to calculate electron transport properties in nanosystems, although calculations of this type are not discussed here.

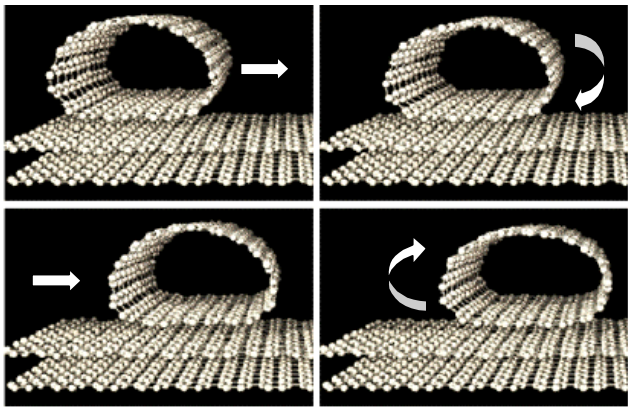

Figure 19 : Snapshots illustrating the sliding-rolling motion observed in a simulation of nanotube moving in registry with the lattice of a graphite substrate.

With their extensive pi bonding and large aspect ratio, nanotubes are expected to have a large and highly anisotropic polarizability, leading to, for example, efficient alignment in applied electric fields. This property suggests the use of nanotubes as switches in nanometer-scale electro-mechanical devices. Alignment in an applied field may also contribute to the field emission measured from nanotube mats, where the alignment of the ends of inter-twined nanotubes with an applied field may enhance field strength and hence help facilitate electron emission from the nanotube ends.

To qualitatively identify trends in dipole moment and polarization energy of nanotubes in applied fields, calculations were carried out of (6,0) nanotubes of various lengths in applied fields of various magnitudes and orientations with respect to the nanotube axis. Plotted in

Fig.20 are the calculated dipole energy $E_d = \boldsymbol{F}\cdot\boldsymbol{d}$ and total energy change per atom, respectively, as a function of field strength for the field aligned with the axis of the nanotube for three nanotubes with different aspect ratios. The longest nanotube simulated contains 288 atoms and is 49.7Å long. Plotted in Fig. 21 are the dipole moment and total energy change per atom as a function of tube length at several field strengths. Plotted in Fig.22 is the dipole energy and total energy change per atom as a function of orientation of the nanotube axis with respect to the direction of the applied field for the highest field strength plotted in Fig.20 (1V/A). The dipole energy and the energy change per atom have roughly a cosine and approximately cosine squared dependence, respectively, on the angle with respect to the applied field direction. The latter results because the polarization energy is dependent on the cosine of the angle of orientation of the dipole moment with respect to the field, and the dipole moment is in turn dependent on the cosine of the orientation angle.

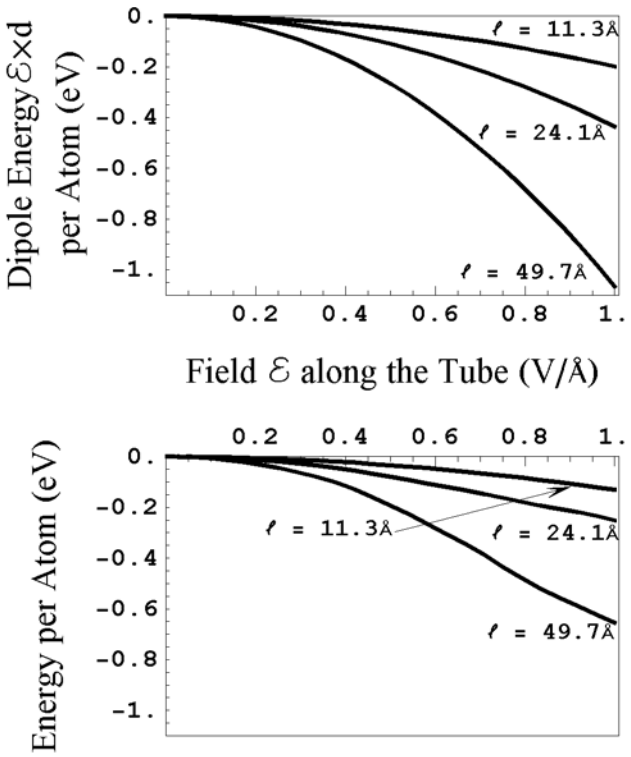

Figure 20 : Calculated dipole energy (calculated as the field times the dipole moment divided by the number of atoms) (top) and total energy change per atom acquired in an applied electric field (bottom) as a function of field strength for the field aligned with the axis of the nanotube for three nanotubes of different lengths.

In principle it is possible that in nanotube mats unconstrained ends of nanotubes could become aligned with an applied field, enhancing the field concentration at the ends and thereby contributing to electron emission. Using the data above, an estimate can be made for the length of nanotube that must be aligned with an applied field such that the polarization energy gained is sufficient to form a kink along the nanotube. Molecular modeling using the bond-order potential described above predicts that kink formation in a single-walled nanotube requires about 30eV. For a field strength of 0.01V/A the minimum length of a (6,0) nanotube that must be aligned with the field to make the polarization energy larger than the energy needed for kink formation is about 20nm. This length is inversely proportional to the field strength, and proportional to the square root of the kink energy.

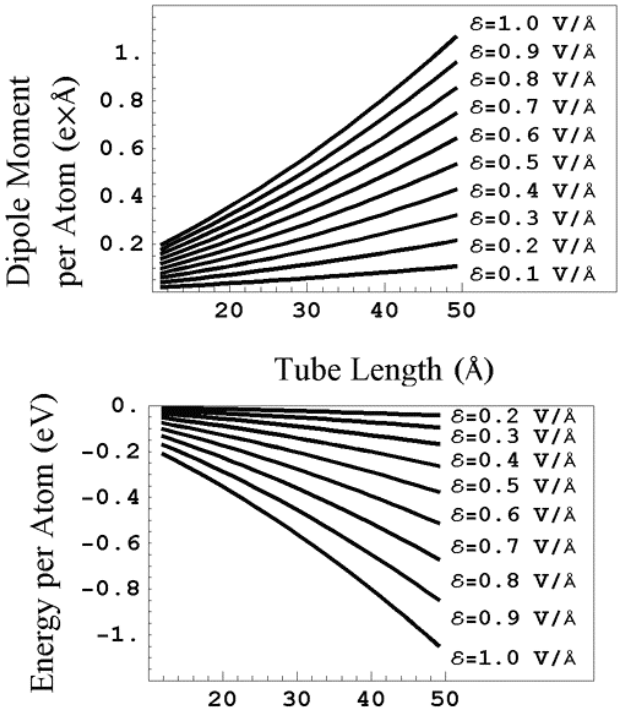

Figure 21 : Dipole moment (top) and total energy change per atom acquired in an applied electric field (bottom) as a function of aspect ratio for several field strengths.

3.1.8 Electrostatic Potentials and Field Emission

Fullerene nanotubes are proving to be robust field emitters for display applications both in highly aligned configurations and as nanotube mats.[Zhu (1999)] From a

theory viewpoint, there is interest in whether these structures can be characterized as ”classical” field emitters or whether they posses unique properties that could potentially be exploited for field-emission applications. For example, in the case of a bulk conductor mobile charge carriers will screen an electric field beyond some thin characteristic skin depth, and therefore all field lines must be perpendicular to the surface. This leads to the field enhancement at protruding surfaces and for high aspect ratio structures. In the case of nanotubes, it is not *a priori* clear that a single layer of carbon atoms is necessarily sufficient to completely screen an applied field. If not, then the assumption of field lines perpendicular to the surface of a nanotube may not be valid, and electron emission from the inner shells of multi-walled nanotubes could be contributing to measured currents. Both would complicate the interpretation of field emission in terms of traditional Fowler-Nordheim behavior. Similarly, it is not clear how well nanotubes in nanotube bundles and mats might screen an applied field from one another, possibly negating some of the advantages associated with using such large aspect ratio structures. Effects such as the alignment of nanotube tips (see above) and mutual screening may contribute to ”flicker” sometimes observed when field-emitting pixels are created from nanotube mats.

Represented by the arrows in Fig. 23 is the potential field surrounding a capped (5,5) nanotube in a field of 0.1 V/A applied parallel to the nanotube axis as predicted by a self-consistent tight-binding calculation. The magnitude and direction of the arrows represent the field strength and orientation, and the solid line represents the outline of the nanotube. The applied field is completely screened in the interior of the nanotube (the residual arrows inside the nanotube are due to the field generated by the nuclei and nanotube electrons, not the applied field), and the field lines are all perpendicular to the nanotube shell. Hence the tight-binding calculation suggests that this structure does indeed act as a classical conductor, a result that is consistent with prior first principles predictions.[Lou (1995)] We note that semiconducting nanotubes should behave as metallic nanotubules when the voltage sweep along the nanotube is larger than the tube band gap. Therefore if a semiconducting nanotube is sufficiently long it should screen the field almost as well as a metallic nanotube. If $E_{BandGap}$ is the bandgap for semiconducting tube and L is the nanotube length, the residual

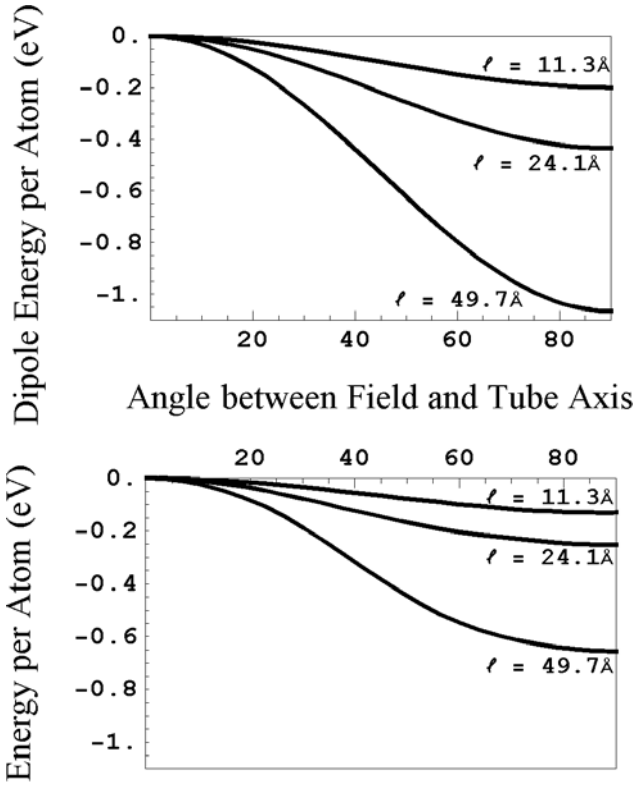

Figure 22 : Dipole energy (top) and total energy change acquired in an applied electric field per atom (bottom) as a function of orientation of the nanotube axis with respect to the direction of the applied field for the highest field strength plotted in Fig.20 (1V/A).

field inside the tube should not exceed $E_{BandGap}$/L.

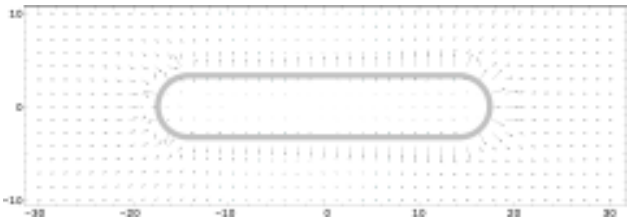

Figure 23 : Representation of the electric field calculated by a self-consistent tight binding method surrounding a capped (5,5) nanotube in an external field of 0.1 V/A applied parallel to the nanotube. The magnitude and direction of the arrows represent the field strength and orientation, respectively, and the solid line represents the outline of the nanotube.

Experimental evidence suggests that the emission thresh-

old voltage for metallic capped single wall nanotubes is about two times lower than that for open ended single-walled nanotubes. [Bonard (1999)] This appears counter intuitive, as the field enhancement should be stronger at the sharper edge of an open-ended nanotube compared to a capped structure. Plotted at the top and bottom of Fig. 24 are grey-scale images that represent the magnitude of the field strength given by the self-consistent tight-binding scheme for the Coulomb potential at the end of a capped and open-ended (5,5) nanotube, respectively, in an applied field of 0.1V/A oriented along the nanotube axis. Plotted at the top and bottom of Fig. 25 is the potential along the edge of the same two structures denoted in Fig.24 under the same conditions of applied field. These results suggest two contributing reasons for the experimental observations regarding emission current. First, although the field enhancement is larger at the open-ended nanotube, the potential barrier for field emission from the nanotube is larger than the capped structure because of the radical states associated with the under-coordinated end carbon atoms. Second, for significant electron emission the states in the vacuum at the end of the nanotube have to be well coupled to the "bulk" states through which electrons are transported in the nanotube. In the case of the capped structure the Fermi levels of the cap and nanotube are almost the same, and the surface states extend into the tube efficiently coupling with the "bulk" states. In the case of the open-ended structure, the surface radical states are highly localized. They are poorly coupled to both vacuum and conducting nanotube states and therefore the nanotube rim serves as an insulator between the vacuum and the nanotube "bulk" states. While there may be high field enhancement at the edge states, the calculations suggest that getting electrons to these states from the tube for emission into the vacuum is not very efficient.

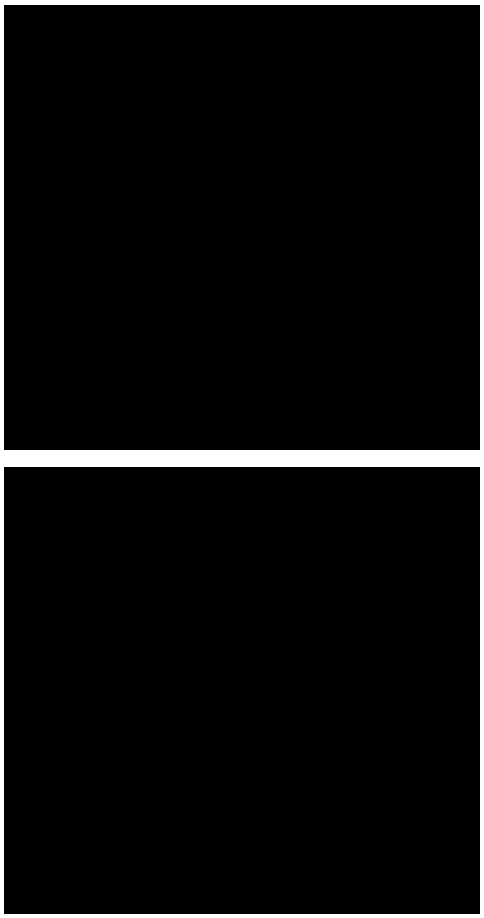

Figure 24 : Grey-scale images representing the Coulomb potential given by the self-consistent tight binding scheme for the potential field at the end of a capped (top) and open-ended (bottom) (5,5) nanotube, respectively, in an applied field of 0.1V/A oriented along the nanotube axis.

4 Diamond Nanoclusters and Nanorods

While not as well studied or perhaps as versatile as fullerene nanotubes, nanodiamond clusters nonetheless have the potential to become important building blocks for nanoscale devices. Nanodiamond clusters are available as detonation products, where they can be found in large amounts with exceptional uniformity and reproducibility. After processing to remove an external disordered carbon shell, nanodiamond cluster sizes created by detonation range in size from two to ten nanometers, with a narrow peak in size distribution at about five nanometers.[Kuznetsov (1998)] While information on the shape of nanodiamond clusters is scarce, diamond particles of micron dimensions are regularly shaped and may exhibit a variety of morphologies including cubo-octahedron, icosahedron and a decahedral-Wulff-polyhedron.

Based on scaling the enthalpies of hydrocarbon molecules to larger scales, it has been suggested that diamond-like clusters containing up to about 3000 carbon atoms are more stable than aromatic structures with comparable hydrogen to carbon ratios (the transitions is predicted to occur at about H/C=0.24).[Badziag (1990)] The stability of diamond over graphitic structures at

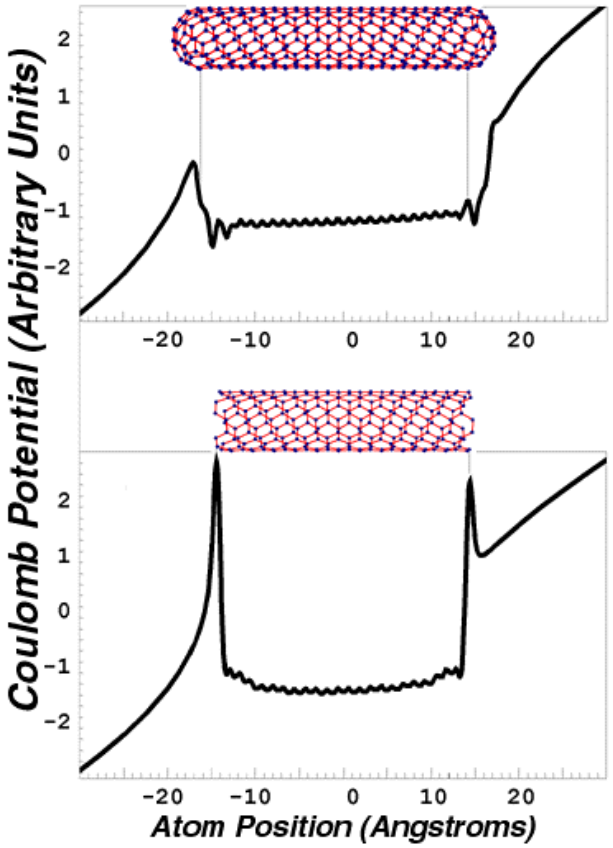

Figure 25 : Coulomb potential along the edge of the same two structures denoted in Fig.24 under the same conditions of applied field. Top: Capped structure. Bottom: Open-ended structure.

small scales is a result of the higher number of surface bonds available in diamond structures on which strong C-H bonds can be formed. This result helps explain why nanodiamond clusters are so readily available as a byproduct of detonation, and suggests that they would be intrinsically stable for nanotechnology applications. Annealing of nanodiamond clusters to temperatures above about 800^oC apparently leads to graphitization.[Chen (1999)] Because the carbon to hydrogen ratio is different for graphitic and diamond-like structures with comparable sizes, high-temperature annealing likely leads to hydrogen desorption that drives the structural transition. For diamond (111) surfaces, thermal programmed desorption measurements indicate loss of hydrogen starting at about 930^oC, followed by reconstruction to a (2x1) pi bond chain structure containing sp^2-bonded surface carbon atoms.[Kubiak (1991)]

Field emission properties of nanodiamond clusters have been studied experimentally, and their low threshold voltages, and relatively high and stable emission currents have made them potential targets for display materials.[Zhirnov (2000)] Directed transport of nanodiamond clusters to the ends of silicon tips and onto graphite surfaces via electrophoresis/dielectrophoresis has been demonstrated. [Alimova (1999)] With their large surface to volume ratio, there has been speculation that the electronic properties of nanodiamond clusters could be tuned by chemisorbing various species to their surface or by subsurface doping with n- and p-type doping elements.[Zhirnov (2000)] The ability to potentially tune their electronic properties together with the directed transport results supports the promise of these structures in technology applications.

The structure and stability of nanodiamond clusters containing 34, 161, 434, 913, 945 and 1602 carbon atoms with shapes that represent those observed for micron-scale structures have been characterized with the bond-order potential. Illustrated in Fig.26 are the structures of each of these clusters. All but the 945 carbon atom clusters have shapes represented by an octahedron containing (111) facets with the top and the bottom vertices cut off to produce (100) surfaces. Plotted in Fig.27 as the open squares are the binding energies for these clusters relative to systems with the same number of carbon atoms in graphite and hydrogen atoms as H_2 molecules given by the bond-order potential as a function of the hydrogen to carbon ratio. These energies were calculated using a dimer reconstruction for all (100) cluster surfaces. Also plotted are comparable data for small hydrocarbon molecules with all sp^3-bonded carbon atoms (open diamonds), benzene and naphthalene (solid squares), and (17,0) nanotubes of different lengths whose ends are hydrogen terminated (solid circles). The energies plotted in Fig. 27 suggest a crossover in stability between graphitic and diamond-like structures for C/H ratios of about three, similar to the value of four predicted by Badziag as discussed above.[Badziag (1990)]

Relationships between various electronic properties and cluster size were explored with the environment dependent tight-binding model discussed above, with C-H terms fit to first principles electronic structure results for ethane, methane, benzene, and hydrogenated $< 111 >$ and $< 100 >$ diamond surfaces. Plotted in Fig. 28 are the density of states for four of the clusters illustrated in

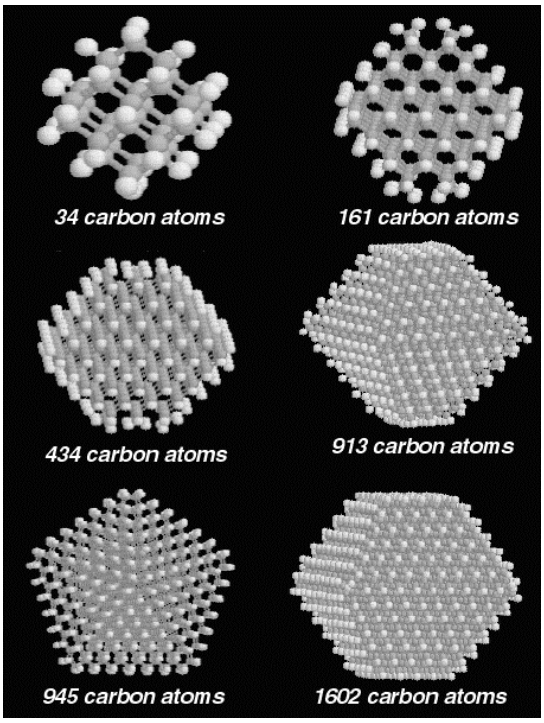

Figure 26 : Illustrations of the nanodiamond clusters studied.

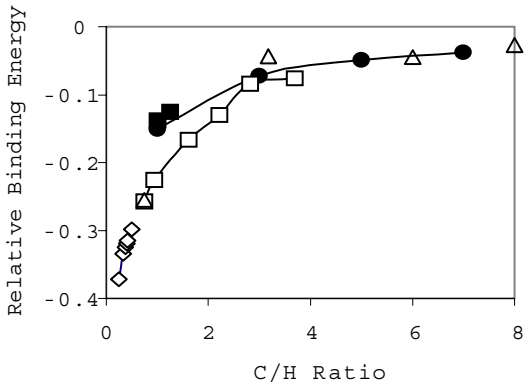

Figure 27 : Binding energies relative to systems with the same number of carbon atoms in graphite and hydrogen atoms as H_2 molecules given by the bond-order potential as a function of the hydrogen to carbon ratio. Open symbols refer to structures in which all carbon atoms are sp^3-bonded; solid symbols refer to sp^2-bonded structures. Energies were calculated using a dimer reconstruction for all surfaces with structures corresponding to the (100) diamond surface. Open diamonds: hydrocarbon molecules (methane, ethane, propane, n-butane, n-pentane, cyclohexane). Open squares: diamond clusters. Open trangles: diamond nanorods. Solid squares: benzene and naphthalene. Solid circles: (17,0) nanotubes of different lengths whose ends are hydrogen terminated.

Fig. 26 and for bulk diamond. The bulk density of states is shifted by the averaged Coulomb potential due to the surface dipole layer (cf. Fig. 29) experienced by carbon atoms in the cluster. All four clusters demonstrate size dependence of the band gap. Dimensional effects are most apparent with respect to the states in the valence band; the highest-occupied molecular orbitals for the 34 and 161 atom clusters lie approximately 2.5 eV and 1.25 eV, respectively, below the bulk valence band edge. At the same time even for the smallest cluster the energy of lowest-unoccupied molecular orbitals coincide with the bulk conduction band edge. This result can be intuitively expected because the states with higher energies and smaller wavelengths are less sensitive to the dimension of the system. Dimensional band gap widening is less than 0.4 eV for the largest cluster examined (913 carbon atom; $\sim$2 nm diameter), which leads to the conclusion that any band gap size effect is insignificant for cluster sizes larger than about 2-2.5 nm. Minor deviations from the bulk spectrum for the largest cluster are mainly due to the presence of hydrogen states, and not to the finite dimensions of the cluster. This result apparently disagrees with indirect X-ray measurements that indicate that in a 3.6 nm cluster the conduction band edge position is 1.2 eV above the conduction band edge for bulk diamond.(Chang (1998) The origin of this apparent discrepancy is not understood.

Coulomb potential distributions for the clusters are plotted in Fig.29. The main feature of the potential distribution is a sharp rise at the cluster surface produced by the hydrogen termination. Cluster size effects are apparently only significant for the smallest cluster. For the larger clusters the potential inside the cluster does not change appreciably with increasing cluster size. In conjunction with the spectra plots the potential rise at the boundary gives a -1.45eV electron affinity of the hydrogenated $<111>$ surface(cf. Fig. 28). That value coincides with the experimentally measured electron affinity [Ristein (2000)], while density functional theory usually overestimates the experimental value by $\sim$0.6-0.8 eV.[Rutter (1998)]

Another class of diamond-based structure that is being explored is diamond nanorods. Four examples with various crystal orientations along their long axis and different surface structures are illustrated in Fig. 30. Indicated in Fig.27 by the open triangles are relative binding energies for these structures as given by the bond-order potential as a function of carbon-to-hydrogen ratio. These energy estimates suggest that diamond nanorods are energetically comparable to finite-sized single-walled nanotubes.

If made, diamond nanorods could potentially find several technologically useful applications, including as fibers in nanocomposites and as resonators. To further explore these possibilities, estimates have been carried out for several of the mechanical properties of these systems. The direction-dependent Young's moduli of bulk diamond, which are given in Tab. 3, should provide reasonable estimates for the corresponding tensile modulus of these systems. The values are comparable to estimates for nanotubes that range from about 0.8 to 1.2 TPa depending on how the cross-sectional area is defined.[Yakobson (1997)]

Because diamond displays brittle fracture behavior, the ideal tensile strength for brittle failure (i.e. failure by which two planes separate uniformly) can be estimated as the maximum in the derivative of the energy with respect to interplanar spacing of the universal binding energy relation of Smith and co-workers.[Rose (1983)] This maximum critical stress $\sigma^m$is given by

$$\sigma^m = (2^{1/2}e)^{-1}[\gamma_c E/d_o]^{1/2} \tag{17}$$

where γ_c and d_0 are the surface energy and inter-planar spacing for planes along which failure occurs, respectively, and E is the tensile modulus in the direction of failure. The predicted critical stress for the diamond nanorods using the data in Tab. 3 as given by Eq.(17) are listed in Tab. 3. These estimates exceed the experimental fracture stress for nanotubes of about 50GPa.[Yu. (2000)] For comparison, recent density functional calculations yield tensile and shear strengths of about 100GPa for bulk diamond. [Roundy (2001)] The prediction from first principles calculations that the shear and tensile yield strengths of diamond are the same suggests that resolved forces that would induce shear modes of failure will not exceed forces needed for separation of planes perpendicular to an applied force for the diamond nanorods.

Estimates have also been made for the fundamental oscillation frequency ω of diamond nanorods and multiwalled carbon nanotubes using the Euler-Bernouilli continuum beam equation for an undamped fixed-end cantilever beam:

$$\omega = \sqrt{\frac{EI}{\rho A}\left(\frac{n\pi}{L}\right)^4} \tag{18}$$

The quantities E and ρ are the modulus and density, respectively, A is the cross sectional area of the beam, n is the mode of oscillation (n= 1 for the fundamental frequency), L is the beam length, and I is the moment of inertia. The moment of inertia for a regular polygonal cross section of n sides is

$$I = \frac{nb^4}{192}\left(\cot\frac{\beta}{2}\right)\left(3\cot^2\frac{\beta}{2}+1\right) \tag{19}$$

where b is the length of a side and β is the central angle for a side. The length of the side b can be described in terms of the circumscribed radius R of the beam.

Table 3 : Predicted properties of diamond nanorods based on diamond bulk properties.

Direction of Nanodiamond Rod Axis	**Tensile Modulus (TPa)**	**Cleavage energy of the corresponding surface (J/m^2)**	**Predicted Tensile Fracture Strength (GPa)**
(001)	1.080	18.8	182
(011)	1.195	11.1	138
(111)	1.239	13.3	131

Plotted in Fig. 31 are calculated oscillation frequencies for diamond nanorods 100 nm in length as a function of radius for several cross-sectional areas. For these calculations, the bulk diamond density (3.52 g/cm^3) and modulus (1 TPa) was assumed. Plotted in Fig.32 is frequency versus circumscribed radius for hexagonal cross section beams of lengths of 50, 100, 150, and 200nm. For comparison, calculated frequencies for nested nanotubes of equivalent lengths are also plotted in Fig.31. In this case, the in-plane modulus (1.1TPa) and bulk

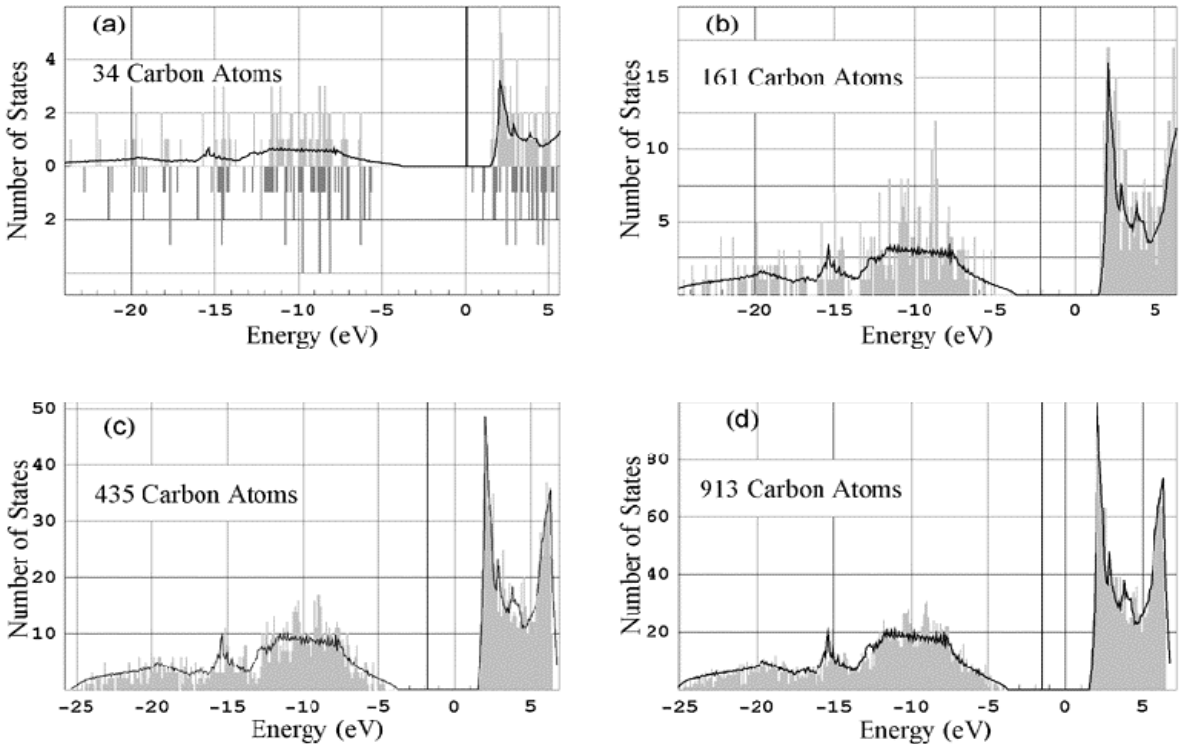

Figure 28 : Electronic density of states for the four smallest clusters illustrated in Fig. 26 (histogram) and for bulk diamond (solid line). The histogram at the bottom of pane (a) is a spectrum generated from density functional theory.

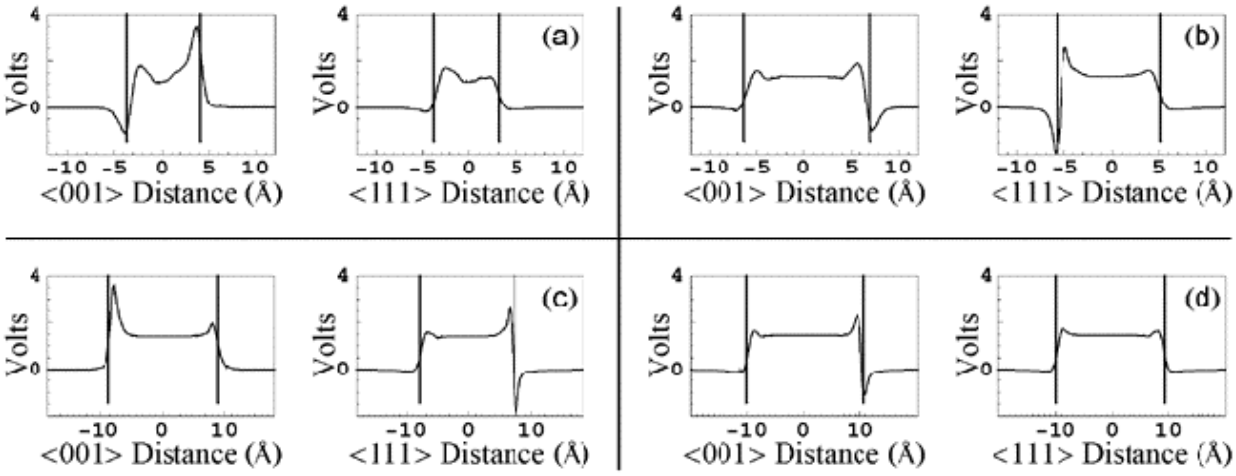

Figure 29 : Coulomb potential distributions for the nanodiamond clusters plotted along the $<100>$ and $<111>$ directions passing through the centers of mass of the clusters.

density of graphite(2.2 g/cm^3) is assumed. According to Eqs. (18) and (19), diamond nanorods will have a slightly lower oscillation frequency than nanotubes due mainly to the higher density of diamond compared to graphite. Nanotubes buckle relatively easily when bent (see above), which could compromise their properties as oscillators for device applications. The response of diamond nanorods to similar distortions is currently being investigated, but it is expected that the diamond structures would not buckle as easily due to their higher density compared to graphite. Depending on their polarizability, diamond nanorods may be superior nano-oscillators for certain technology applications.

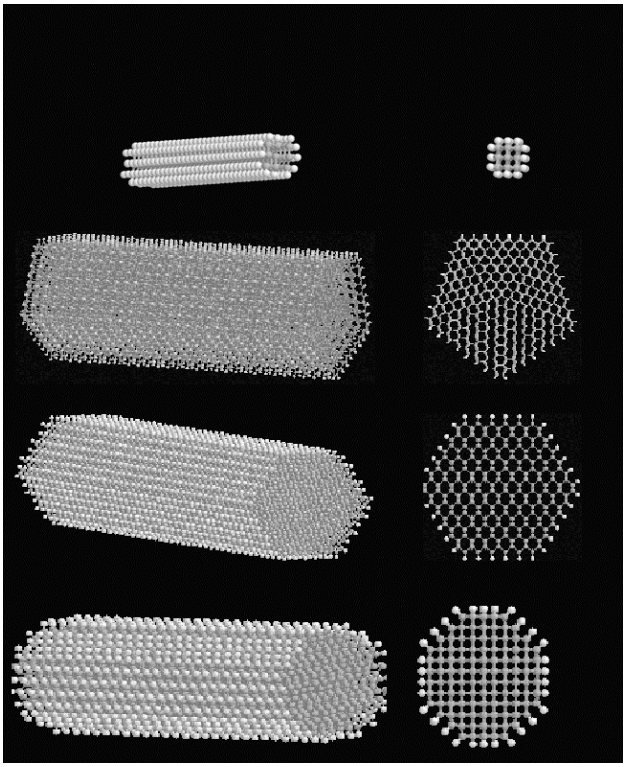

Figure 30 : Illustrations of some example diamond nanorods. Top: Principle axis of the nanorod corresponds to the diamond $<001>$ direction, (001) facets. Upper Middle: Principle axis of the nanorod corresponds to the diamond $<011>$ direction, (001) facets. Lower Middle: Principle axis corresponds to diamond $<011>$, (001) and (111) facets. Bottom: Principle axis corresponds to diamond $<001>$, (011) and (001) facets.

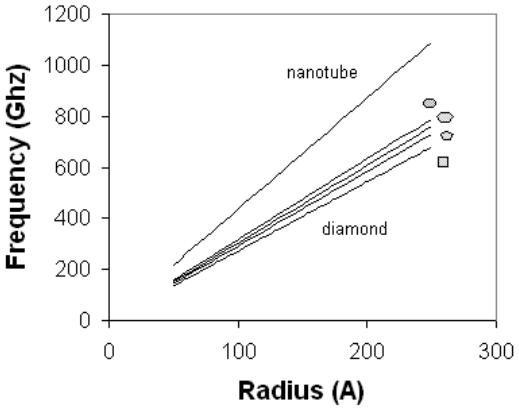

Figure 31 : Calculated oscillation frequencies for a nested nanotube and diamond nanorods with several cross-sectional areas as a function of radius. A length of 50nm is assumed for each system.

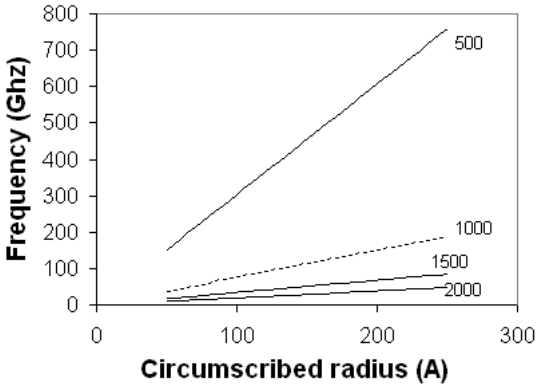

Figure 32 : Frequency versus circumscribed radius for hexagonal cross section diamond nanorods for lengths of 50, 100, 150, and 200nm.

4.1 Hybrid Diamond-Nanotube Structures

There is a geometrical similarity between the $\{111\}$ planes of diamond and individual graphene sheets in which pairs of diamond planes resemble "puckered" graphite. This relationship, together with the lengthening of carbon-carbon bonds from 1.42 Å in graphite to 1.54 Å in diamond, results in the near epitaxial relations

$$\text{Graphite } (0001) \,||\, \text{diamond } (111)$$

$$\text{Graphite } [11\bar{2}0] \quad ||\, \text{diamond } [10\bar{1}]$$

between graphite and diamond planes. These relations have been utilized in several models for understanding important structures and processes in carbon materials, including diamond nucleation on graphite[Lambrecht (1993)] and graphitization of diamond surfaces and clusters.[Davidson (1994); Kuznetsov (1998)]

There are also similar but less obvious relations between fullerene nanotubes and diamond that lead to a number of mechanically and chemically stable structures with potential structural materials and nanoelectronic device applications. Guidelines for creating a range of robust nanotube-diamond structures have recently been developed and tested with the bond-order potential. These geometrical guidelines are surveyed below. The analysis is restricted to (n,0) and (n,n) nanotubes perpendicularly attached to diamond (001) and (111) facets.

Particular classes of (n,0) nanotubes can be chemically attached to diamond (111) facets with strong bonds and low residual stresses. The distance between sites available for bonding a^T at the edge of a (n,0) nanotube depends on the nanotube parameter n as

$$a^T = \frac{\sqrt{3}a^{Gr}n}{\pi}\sin\frac{\pi}{n} \tag{20}$$

where a^{Gr}=2.46 Å is the second neighbor distance of graphene. Due to the hexagonal arrangement of atoms available for bonding on the (111) diamond surface, it is possible to connect bonding sites in the shape of a polygon with any number of segments N (starting with N=3) of equal lengths a^D=2.52 Å. Depending on N, angles at the vertices of the corresponding polygons can vary. To create a strong chemical interface between a (n,0) nanotube and the corresponding N-sided polygon formed by dangling bonds on a diamond surface, the shape of the polygon should be as close to circular as possible to match that of a nanotube edge. Using Eq.(19), the total mismatch between a nanotube of perimeter L_T and the perimeter of a polygon on the diamond surface L_D can be evaluated as

$$\delta_{tot} = \frac{L_D - L_T}{L_D} = \frac{a^D - a^T}{a^D} \tag{21}$$

In addition to total mismatch, a local mismatch can be defined as the distance between a single vertex of a polygon on a diamond surface and the point of the projection of a corresponding atom from a nanotube edge. Atomic level simulations have suggested that local lateral mismatches as large as about 1 Å do not necessarily inhibit strong bond formation.

Based on criteria related to the total and local mismatches, six distinct groups of (n,0) nanotubes with different degrees of bond formation with a diamond (111) facet can be identified depending on the parameter n. The first two distinct groups correspond to nanotubes with six-fold *(6xM,0)* and three-f old *(6xM+3,0)* symmetry where M is an integer. The bonding mismatches for these two groups are relatively small for small radii structures. At larger radii, the *(6xM,0)* structures may have relatively large local bonding mismatches, but these can be easily accommodate by deformations of the nanotubes. Therefore both of these geometrical groups can form particularly strong interfaces.

The second two groups of nanotubes are denoted by *(6xM+2,0)* and *(6xM+4,0)*. The polygons corresponding to bonding of these groups on a diamond (111) facet posses two-fold symmetry, and because the shape of the diamond polygons is elongated along one of their diameters, the tube shape near the interface becomes elliptic. The degree of distortion away from circular is larger for small radii nanotubes, and therefore the stability of the interface for these groups of nanotubes increases with increasing radius. The two final groups of nanotubes, the geometry for which can be described as *(6xM+1,0)* and *(6xM-1,0)*, will have dangling bonds. The shapes of the corresponding polygons are irregular and significantly deviate from circular along one of their sides. Not being completely flexible, nanotubes cannot accommodate such distortions, and the interface energies are relatively high.

The symmetry of (n,n) nanotubes do not match well with that of a defect-free diamond (111) facet, and therefore interfaces of this type will not in general show strong bonding. However, there is a strong similarity between the five-fold symmetric (111) facets of the diamond pentaparticle discussed above and ends of *(5xM, 5xM)* nanotubes that can result in strong bonding. A model interface of this type for a (5,5) nanotube is illustrated in Fig. 33. Due to the defected structure of a pentaparticle, the outer region of the structure is under tension. This stress results in an increasing distance between surface atoms the further they are from the center of the structure. The result is an increase in mismatch for this struc-

ture as the nanotube radius increases. The simulations predict that the local mismatch can be accommodated at least for nanotubes up to M=3.

Because of the four-fold symmetry of (100) diamond facets, a general scheme like that outlined above for the attachment of nanotubes to (111) facets could not be developed. Analysis of bonding geometries together with molecular modeling studies, however, has been able to identify specific cases of strong bonding. One such example, a (8,0) nanotube attached to the (100) facet of a diamond cluster, is illustrated in Fig. 34. The total mismatch between the surface sites and the nanotube is only 4.9%, and the simulations predict that the local mismatch of 0.49 Å can be easily accommodated by the nanotube.

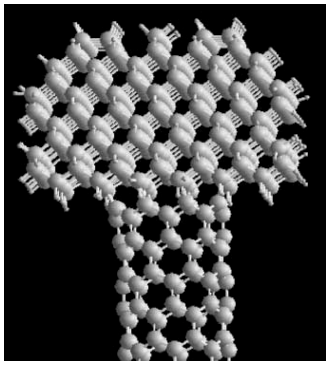

Figure 34 : Illustration of a (8,0) nanotube attached to the (100) facet of a diamond cluster.

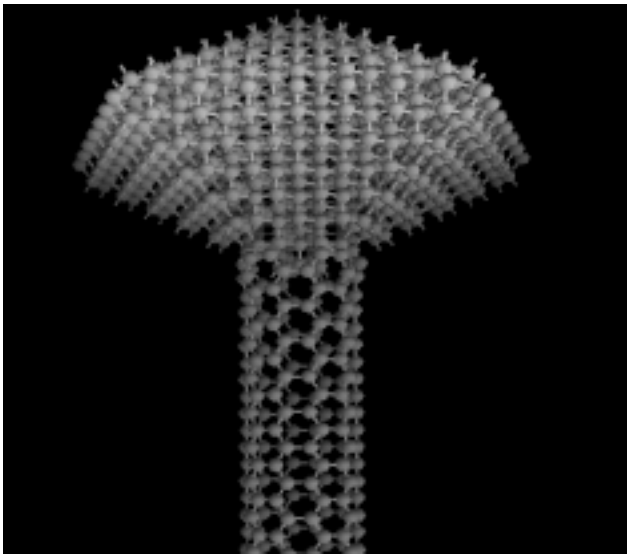

Figure 33 : Illustration of an interface between a (5,5) nanotube and a diamond pentaparticle.

5 Some Unanswered Questions and New Directions

The intent of this paper is to survey recent modeling and theory studies that were aimed at addressing issues related to applications of carbon-based nanostructures in new technologies. Issues related to those addressed above but that have yet to be fully addressed include the following:

Thermal energy transfer in nanotubes/polymer composites: The issue of load transfer between a polymer matrix and nanotube via chemical cross-links was addressed above. Similarly, for thermal management applications, there must be strong thermal (i.e. phonon) coupling between the matrix and nanofibers. However, weak bonding between the two systems will likely inhibit strong thermal coupling, which together with the possibility of localized vibrational modes associated with defects in nanotubes would likely compromise the thermal energy transfer in the composite. Studies involving classical motion of atomic species such as molecular dynamics simulations can start to address some of these issues, for example how cross-links could help matrix-nanofiber thermal coupling, and whether scattering from cross-link sites would lower the phonon mean free path in nanotubes and therefore reduce their thermal conductivity. For quantitative studies of phonon coupling, however, quantum mechanical phonon descriptions will probably be needed. In this area vibrational energy transfer methods developed primarily for molecular systems could be useful.

Mutual screening and field-induced desorption from nanotubes: There are issues related to field emission from fullerene nanotubes that were not discussed above but that nonetheless play a potentially important role in the technological development of these systems. For example, in the case of nanotube mats and bundles of well-aligned nanotubes, screening of the applied field by two or more adjacent nanotubes may reduce field enhancement expected for a single nanotube in the same applied field. The results above suggest that nanotubes act like ideal conductors, and therefore in principle the magnitude of a field inside of a collection of nanotubes as a function of applied external field could be approximated using classical electrostatics. Field evaporation of carbon from the ends of nanotubes likely contributes to the

lifetime of a nanotube field emitter. The environment dependent tight-binding model in which the self-consistent terms are included yields a total potential energy that can be used in molecular simulations. Although mainly electronic structure predicted by our tight-binding model has been discussed, the model can also be adapted to predict total energies in an applied field, and therefore could be used to predict rates for field evaporation as a function of structure and field strength.

Surface doping of nanodiamond clusters: The large surface-to-volume ratio together with the prediction that surface electronic states in nanodiamond clusters are near the Fermi level suggests that these structures could be doped by surface chemisorption. Calculations of the states introduced by particular adsorbing species, together with predictions of their thermodynamic and kinetic stability appears to be a ripe area for theory, especially first principles calculations.

Biological activity: As mentioned in the introduction, the biological activity of the C_{60} molecule is being aggressively studied, and progress in developing drugs based on C_{60} for treating AIDS and neurodegenerative diseases has been reported. Could nanotubes, or even nanodiamond clusters, especially those that are functionalized, have similar biological activity? Molecular modeling studies pointed toward the biological activity of C_{60} as an anti-viral drug for the treatment of AIDS.[Mi (1999)] Similar studies using finite nanotubes and nanodiamond clusters could prove effective in identifying similar biological activity of these unique nanostructures.

Acknowledgement: Several of the studies discussed above were carried out with collaborators, and the authors are grateful to have had a chance to work with these individuals. They include Kevin Ausman, Alper Buldum, Attila Caglar, Mike Falvo, Michael Griebel, John Hren, Ben Lawson, J.-P. Lu, James Mewkill, Rod Ruoff, Susan Sinnott, Deepak Srivastava, Josh Steele, Richard Superfine, Russell Taylor, Sean Washburn, M.F. Yu, Victor Zhirnov, and Otto Zhou. Discussions with Jerzy Bernholc, Marco Buongiorno Nardelli, Brett Dunlap, Judith Harrison, Richard Jaffe, John Mintmire, John Pazik, Christopher Roland, P.P. Schmidt, C.T. White and Boris Yakobson are also gratefully acknowledged. Funding for the work described above came primarily from the Office of Naval Research through a Multi-University Research Initiative and the NASA-Ames Computational Nanotechnology Program. DWB would also like to acknowledge the National Science Foundation and the Department of Energy for support.

References:

Abell, G.C. (1985): Empirical Chemical Pseudopotential Theory of Molecular and Metallic Bonding. *Phys. Rev. B*. vol. 31, pp. 6184-6196.

Ajayan, P.M.; Schadler, L.S.; Giannaris, C.; Rubio, A. (2000): Single-walled carbon nanotube-polymer composites: Strength and weakness. *Adv. Materials*, vol. 12, p. 759.

Alimova, A.N.; Chubun, N.N.; Belobrov, P.I. ; Detkov, P.Y.; Zhirnov, V.V., (1999): Electrophoresis of Nanodiamond Powder for Cold Cathode Fabrication. *J.Vac.Sci.Technol.* vol. B17, pp.715-720.

Andrews, R.; Jacques, D.; Rao, A.M., Rantell, T.; Derbyshire, F.; Chen, Y.; Chen, J.; Haddon, R.C. (1999): Nanotube composite carbon fibers. *Appl. Phys. Lett*. Vol. 75, pp. 1329-1332.

Areshkin, D. (2002): Ph.D. Thesis (in progress).

Badziag, P.; Verwoerd, W.S.; Ellis, W.P.; Greiner, N.R. (1990): Nanometre-Sized Diamonds are more Stable than Graphite. *Nature*, vol. 343, pp. 244-245.

Badziag, P.; Verwoerd, W.S.; Ellis, W.P.; Greiner, N.R. (1990): Nanometre-Sized Diamonds are more Stable than Graphite. *Nature*, vol. 343, pp. 244-245.

Bernholc, J.; Brenner, D.; Buongiorno Nardelli, M.; Meunier, V.; Roland, C. (2002): Mechanical and Electrical Properties of Nanotubes. *Annual Review of Materials Research*, vol. 32, in press.

Bonard, J.M.; Salvetat, J. P.; Stöckli, T.; Forró, L.; Châtelain, A. (1999): Field Emission from Carbon Nanotubes: Perspectives for Applications and Clues to the Emission Mechanism. *Applied Physics A*, vol. 69, pp. 245-250.

Brenner, D.W. (1989): Relationship Between the Embedded-Atom Method and Tersoff Potentials. *Phys. Rev. Lett.* vol. 63, p. 1022.

Brenner, D.W. (1990): Empirical Potential for Hydrocarbons for Use in Simulating the Chemical Vapor Deposition of Diamond Films. *Phys. Rev. B, v*ol. 42, pp. 9458-9471.

Brenner, D.W. (2000) The Art and Science of an Analytic Potential. *Physica Status Solidi* B, vol. 217, pp.

23-40.

Brenner, D.W.; Shenderova, O.A.; Areshkin, D.A. (1998a): Quantum-Based Analytic Interatomic Forces and Materials Simulation. *Reviews in Computational Chemistry*, K.B. Lipkowitz and D.B. Boyd, Eds., (VCH Publishers, New York, 1998), pp 213-245.

Brenner, D.W.; Shenderova, O.A.; Harrison, J.A.; Stuart, S.J.; Ni, B.; Sinnott, S.B. (2002): Second Generation Reactive Empirical Bond Order Potential Energy Expression for Hydrocarbons. *J. Phys.: Solid State*, in press.

Brenner, D.W.; Schall, J.D.; Mewkill, J.P.; Shenderova, O.A.; Sinnott, S.B. (1998b): Virtual Design and Analysis of Nanometer-Scale Sensor and Device Components. *Journal of the British Interplanetary Society,* vol. 51, pp. 137-142.

Chang, Y. K. ; Hsieh, H. H.; Pong, W. F.; Tsai, M. H.; Chien, F. Z.; Tseng, P. K.; Chen, L. C.; Wang, T. Y.; Chen, K. H.; Bhusari, D. M.; Yang, J. R. and Lin, S. T. (1998): Quantum Confinement Effect in Diamond Nanocrystals Studied by X-Ray-Absorption Spectroscopy. *Phys. Rev. Lett.* vol. **82**, pp. 5377-5380.

Chen, P.;Wu, X.; Lin, J.; Tan, K.L. (1999): High H-2 uptake by alkali-doped carbon nanotubes under ambient pressure and moderate temperatures. *Science*, vol. 285, pp. 91-93.

Chen J.; Deng S.Z.; Chen J.; Yu Z.X.; Xu N.S. (1999): Graphitization of Nanodiamond Powder Annealed in Argon Ambient. *Appl. Phys. Lett.*, vol. 74, pp. 3651-3653.

Chico,L.; Crespi, V.H.; Benedict, L.X.; Louie, S.G.; Cohen, M.L. (1996): Pure Carbon Nanoscale Devices: Nanotube Heterojunctions. *Phys. Rev. Lett*. vol. 76, pp.971-974.

Darkrim, F.; Levesque, D. (1998): Monte Carlo simulations of hydrogen adsorption in single-walled carbon nanotubes. J. Chem. Phys. Vol. 109, pp. 4981-4984.

Davidson, B.N.; Pickett, W.E. (1994): Graphite-layer Formation at a Diamond (111) Surface Step. *Phys. Rev. B*, vol 49, pp. 14770-14773.

Demkov, A.A.; Ortega, J.; Sanky, O.F.; Grumbach, M.P.(1995): Electronic Structure Approach for Complex Silicas. *Phys. Rev. B*, vol. 52, pp.1618-1630.

Dillon, A.C.; Jones, K.M.; Bekkedahl, T.A.; Kiang, C.H.; Bethune, D.S.; Heben, M.J., (1997): Storage of Hydrogen in Single-Walled Carbon Nanotubes. *Nature*, vol. 386, pp. 377-379.

Dresselhaus, M.S.; Dresselhaus, G; and Eklund, P.C. (1996): *Science of Fullerenes and Carbon Nanotubules*, (Academic Press, San Diego).

Elert, M.L.; White, C.T.; Mintmire, J.W. (1985): Conformation and Electronic Properties of Helical CIS-polyacetylene. *Mol. Cryst. Liq. Cryst.* vol. 125, pp.329-335.

Falvo, M.R., Steele, J.; Buldum, A.; Schall, J.D.; Taylor II, R.M., Lu, J.P.; Brenner, D.W.; Superfine, R. (2002): Observation of Nanometer-Scale Rolling Motion Mediated by Commensurate Contact. *J. Phys. Conds. Matter*, in press.

Falvo, M.R.; Steele ,J.; Taylor, R.M.; Superfine, R. (2000): Gearlike Rolling Motion Mediated by Commensurate Contact: Carbon Nanotubes on HOPG. *Phys. Rev. B.* vol. 62, pp. R10665-R10667

Field, J.E. (1992): The Properties of Natural and Synthetic Diamond. (Academic, London)

Foulkes, W.M.C.; Haydock, R., (1989): Tight-Binding Models and Density Functional Theory. *Phys. Rev. B.* vol. 39, pp. 12520-12536.

Frankland, S.J.V.; Brenner, D.W. (2001): Hydrogen Raman Shifts in Carbon Nanotubes from Molecular Dynamics Simulation. *Chem. Phys. Lett*. vol. 334, 18-23.

Frankland, S.J.V.; Caglar, A.; Brenner, D.W.; Griebel, M. (2002): Molecular Simulation of the Influence of Chemical Cross-Links on the Shear Strength of Carbon Nanotube-Polymer Interfaces. unpublished.

Frankland, S.J.V., Caglar, A.; Brenner, D.W.; Griebel, M. (2002): Molecular Simulation of the Influence of Chemical Cross-Links on the Shear Strength of Carbon Nanotube-Polymer Interfaces. submitted.

Frauenheim T.; Seifert G.; Elstner M.; Hajnal Z.; Jungnickel G.; Porezag D.; Suhai S.; Scholz R. (2000): A self-consistent charge density-functional based tight-binding method for predictive materials simulations in physics, chemistry and biology. *Physica Status Solidi B*, vol 217, pp. 41-62.

Garg, A.; Sinnott, S. B. (1998): Effect of Chemical Functionalization on the Mechanical Properties of Carbon Nanotubes. *Chem. Phys. Lett*. vol. 295, pp. 273-278.

Givargizov, E.I.; Zhirnov, V.V.; Stepanova, A.N.; Rakova, E.V.; Kiselev, A.N.; Plekhanov, P.S. (1995):

Microstructure and Field-Emission of Diamond Particles on Silicon Tips. *Appl. Surf. Sci.* vol. 87-8, pp. 24-30.

Hadjiev, V.G.; Iliev, M.N.; Arepalli, S.; Nikolaev, P.; Files, B.S. (2001): Raman scattering test of single-wall carbon nanotube composites. *Appl. Phys. Lett*. vol. 78, pp. 3193-3195.

Harris, J. (1985): Simplified Method for Calculating the Energy of Weakly Interacting Fragments. *Phys. Rev. B.* vol. 31, pp. 1770-1779

Horsfield A.P.; Bratkovsky A.M. (2000): Ab initio tight binding. *J. Chem. Phys.* vol. 12, pp. R1-R24.

Hynek, S.; Fuller, W.; Bentley, J. (1997): Hydrogen Storage by Carbon Sorption. *Int. J. Hydrogen Energy,* vol. 22, pp. 601-610.

Iijima, S.; Brabec, C.; Maiti, A.; Bernholc, J. (1996): Structural Flexibility of Carbon Nanotubes. *J. Chem. Phys*. vol. 104, pp. 2089-2092.

Iijima, S. (1991): Helical Microtubules of Graphitic Carbon. *Nature* Vol. 354, pp. 56-58.

Jensen, A. W.; Wilson, S. R.; Schuster, D. I. (1996): Biological Applications of Fullerenes -A Review. Bioorg. Med. Chem. vol. 4, 767-779.

Kubiak, G.D.; Hamza, A.V.; Stulen, E.; Sowa, E.C.; Kolasinski, K.W. (1991): Hydrogen Desorption and Subsequent Reconstruction of Natural Diamond Surfaces, in *New Diamond Science and Technology*, R. Messier, J.T. Glass, J.E. Butler and R. Roy, editors (Materials Research Society, Pittsburgh, 1991).

Kuznetsov, V.L; Chuvilina, A.L.; Butenkoa, Y.V.; Stankusb, S.V.; Khairulinb, R.A.; Gutakovskiic, A.K. (1998): Closed Curved Graphite-Like Structures Formation on Micron-Size Diamond. *Chem. Phys. Lett*. vol. 289, pp. 353-360 and references therein.

Lambrecht, W.; Lee,C.H.; Segall, B.; Angus, J.C.; Li, Z.; Sunkara, M. (1993): Diamond Nucleation by Hydrogenation of the Edges of Graphitic Precursors. *Nature*, vol. 364, pp. 607-610.

Lou, L.; Nordlander, P.; Smalley, R.E. (1995): Fullerene nanotubes in electric fields. *Phys. Rev. B*, vol. 52, pp.1429-1431.

Louie, S.G.; Chelikowsky, J.R.; Cohen, M.L. (1977): Ionicity and the Theory of Schottky Barriers. *Phys. Rev. B*, vol. 15, pp.2154-2162.

Lordi, V.; Yao, N. (2000): Molecular Mechanics of Binding in Carbon-Nanotube-Polymer Composites. *J. Mater. Res.* vol. 15, pp. 2770-2779.

Mi, H.; Tuckerman, M. E.; Schuster, D. I.; Wilson, S. R. (1999): A Molecular Dynamics Study of HIV-1 Protease Complexes with C60 and Fullerene-Based Anti-Viral Agents. *Proc. Electrochem. Soc.* PV 99-12, pp. 256-269.

Mintmire, J.W; Dunlap, B.I.; White, C.T. (1992): Are Fullerene Tubules Metallic?, *Phys. Rev. Lett*. vol. 68, pp. 631-634.

Nutzenadel, C.; Zuttel, A.; Chartouni, D.; Schlapbach, L. (1999): Electrochemical Storage of Hydrogen in Nanotube Materials. *Electrochemical and Solid State Letters*, vol. 2, pp. 30-32.

Paulson, S.; Helser, A.,; Nardelli, M.B.; Taylor, R.M.; Falvo, M.; Superfine, R.; Washburn, S. (2000): Tunable Resistance of a Carbon Nanotube-Graphite Interface. *Science*, vol. 290, pp.1742-1744.

Qian, D.; Dickey, E.C.; Andrews, R.; Rantell, T. (2000): Load transfer and deformation mechanisms in carbon nanotube-polystyrene composites. *Appl. Phys. Lett*. vol. 76, pp. 2868-2870.

Ristein, J. (2000): Electronic properties of diamond surfaces - blessing or curse for devices? *Diamond and Related Materials*, vol. 9, pp. 1129-1137.

Rose, J.H.; Smith, J.R.; Ferrante, J. (1983), Universal Features of Bonding in Metals. *Phys. Rev. B*, vol. 28, pp. 1835-1845.

Roundy, D.; Cohen. M.L. (2001): Ideal strength of diamond, Si, and Ge. *Phys. Rev. B*, vol . 64, pp. 212103-212106.

Rutter, M.J. and Robertson, J. (1998): Ab initio calculation of electron affinities of diamond surfaces. *Phys. Rev. B*, vol. 57, pp. 9241-9245.

Schall, J.D.; Brenner, D.W. (2000): Molecular Dynamics Simulations of Carbon Nanotube Rolling and Sliding on Graphite. *Molecular Simulation*, vol. 25, pp. 73-79.

Shenderova, O.A.; Lawson, B.W., Areshkin, D.; Brenner,D.W. (2001): Predicted Structure and Electronic Properties of Individual Carbon Nanocones and Nanostructures Assembled from Nanocones. *Nanotechnology*, vol 12, 191-197.

Siefert, G.; Kohler, T.; Frauenheim,T. (2000): Molecular wires, solenoids, and capacitors and sidewall functionalization of carbon nanotubes. *App. Phys. Lett*. vol 77, pp 1313-1315.

Simonyan, V.V.; Diep, P.; Johnson,J.K., (1999): Molecular simulation of hydrogen adsorption in charged single-walled carbon nanotubes *J. Chem. Phys*. vol. 111, pp. 9778-9783.

Srivastava, D.; Brenner, D.W.; Schall, J.D.; Ausman, K.D.; Yu, M.F.; Ruoff, R.S. (1999): Predictions of Enhanced Chemical Reactivity at Regions of Local Conformation Strain on Carbon Nanotubes: Kinky Chemistry. *J. Phys. Chem. B,* vol. 103, pp. 4330-4337.

Sutton, A.P. (1993): *Electronic Structure of Materials* (Clarendon Press, Oxford).

Tang, M.S.; Wang, C.Z.; Chan, C.T.; Ho, K.M. (1996): Environment-dependent tight-binding potential model. *Phys. Rev. B,* vol. 53, 979-982.

Tersoff, J. (1986): New Empirical Model for the Structural Properties of Silicon. *Phys. Rev. Lett*. vol. 56, pp. 632-635.

Wagner, H. D.;Lourie, O.; Feldman, Y.; Tenne, R. (1998): Stress-Induced Fragmentation of Multiwall Carbon Nanotubes in a Polymer Matrix. *Appl. Phys. Lett*. vol. 72, pp. 188-190.

Wang, Q.; Johnson, J.K. (1999): Computer simulations of hydrogen adsorption on graphite nanofibers. *J. Phys. Chem. B,* vol. 103 pp. 277-281.

White, C.T.; Robertson, D.H., Mintmire, J.W. (1993): Helical and Rotational symmetries of Nanoscale Graphitic Tubules. *Phys. Rev. B,* vol. 47, pp.5485-5488.

White, C.T.; Todorov, T.N. (1998): Carbon Nanotubes as Long Ballistic Conductors. *Nature,* vol. 6682, pp. 240-242.

Wood, J.R.; Zhao, Q.; Frogley, M.D.; Meurs, E.R.; Prins, A.D.; Peijs, T.; Dunstan, D.J.; Wagner, H., (2000): Carbon nanotubes: From molecular to macroscopic sensors. *Phys. Rev. B,* vol. 62, 7571-7575

Yakobson, B.I.; Smalley, R.E. (1997): Fullerene Nanotubules: C1,000,000 and Beyond. *American Scientist,* vol 85 pp.324-337.

Ye, Y.; Ahn, C. C.; Witham, C.; Fultz, B; Liu, J.; Rinzler, A. G.; Colbert, D.; Smith, R. Smalley, R.E. (1999): Hydrogen adsorption and cohesive energy of single-walled carbon nanotubes. *Appl. Physics Lett.*, vol. 74 pp. 2307-2309.

Yu, M. F.; Files, B. S.; Arepalli, S.; Ruoff, R. S. (2000): Tensile Loading of Ropes of Single Wall Carbon Nanotubes and their Mechanical Properties. *Phys. Rev. Lett*. vol 84. pp. 5552-5555.

Zhao, Q.; Wood, J.R.; Wagner, H.D. (2001): Stress fields around defects and fibers in a polymer using carbon nanotubes as sensors. *Appl. Phys. Lett.* vol. 78, pp. 1748-1750.

Zhirnov, V. (2000): Private Communication.

Zhirnov, V.V.; Hren J.J. (1998): Electron emission from diamond films. *Mat. Res. Soc. Bulletin,* vol. 23, pp. 42-48 and references therein.

Zhu W.; Bower, C.; Zhou O.; Kochanski G.; Jin, S. (1999): Large Current Density from Carbon Nanotube Field Emitters. *Appl. Phys. Lett*. vol. 75, pp. 873-875.